Russian Chemical Reviews **76** (6) 553 – 581 (2007) © 2007 Russian Academy of Sciences and Turpion Ltd

DOI 10.1070/RC2007v076n06ABEH003721

Modern trends in the development of surface science as applied to catalysis. The elucidation of the structure – activity relationships in heterogeneous catalysts

V I Bukhtiyarov

Contents

I.	Introduction	553
II.	The 'pressure gap' problem	555
III.	The 'material gap' problem	564
IV.	Investigations into the structure of active sites in porous catalysts	570
V.	Development of methods of the purposeful synthesis of highly active catalysts	575
VI.	Conclusion	578

Abstract. A fundamental approach to the development of heterogeneous catalysts consisting of the study of the structure – activity relationships using surface science methods and techniques is proposed. According to this approach, a study should start with an investigation into well-ordered single crystals under ultrahigh vacuum conditions and then move along the way of both increasing the gas phase pressure (to address the 'pressure gap' problem) and complicating the samples under study from single crystals to supported clusters (to address the 'material gap' problem). The case studies cited in the review prove the efficacy of the proposed approach to investigations into the reactivity of active component particles for the subsequent molecular design of catalysts with improved performance (activity, selectivity and stability) and demonstrate that it conforms with the modern trends in the development of surface science as applied to heterogeneous catalysis. The bibliography includes 198 references.

I. Introduction

Traditionally, the term 'Surface Science' implies the application of specific instrumental techniques that are intrinsically surface sensitive to studies of the surface structure and composition of solids. In contrast to standard analytical techniques, such methods yield information on a few surface layers (with a thickness of up to 10 nm) of a sample rather than on its total bulk. The tremendous progress in this field started in the 1970s when serial ultrahigh vacuum spectometers equipped with one or several surface science techniques appeared on the market. That time, Auger electron spectroscopy (AES), low-energy electron diffraction (LEED), X-ray and UV photoelectron spectroscopy (XPS and UPS, respectively), electron energy loss spectroscopy (EELS) were among the most popular techniques. Their wide utilisation in the practice of the experimental studies of solid surfaces enabled the retrieval of important information at the atomic or molecular level. Fundamentals of instrumental techniques for surface studies (ITSS) as well as specific examples of their application, which demonstrate general trends in this field by the end of the 20th century are nicely described in a series of reviews published in 1994 in a special issue of the journal 'Surface Science' devoted to its 30th anniversary.[1]

As applied to catalysis, it is the interactions between simple gases (*e.g.*, CO, O_2, NO, C_2H_4, *etc.*) and clean single-crystalline metal surfaces (Pt, Pd, Ag, Cu) that were the central problem of surface science in that period (see Refs 2 – 4 and references therein). These studies gave rise to the identification of a large number of adsorbed species, which helped to rationalise diverse surface phenomena, such as physical and chemical adsorption, lateral interactions in adsorbed monolayers and chemical interactions on surfaces.

The results obtained were immediately appreciated by specialists in catalysis such that the knowledge gathered on the 'intimate' life of atoms and molecules became a basis for the improvement on the performance of catalysts. Since then, attempts at the molecular design of catalysts with improved characteristics were often preceded by in-depth elucidations of the interactions between the reaction media and smooth solid surfaces in order to understand the nature of the catalytic action of specific active components in specific catalytic reactions. Recently, such an approach referred to as the fundamental one in contrast to the empirical approach became very popular.

Despite the fact that ITSS provide detailed information at the atomic and molecular levels, their efficient application to the description of real catalytic processes is hindered by two major factors commonly referred to as 'pressure gap' and 'material gap'. The former problem consists of the difference in pressures typical of the majority of surface science studies ($P \leqslant 10^{-6}$ mbar) and of real catalytic processes ($P \geqslant 1$ mbar). As a result, concentrations of important intermediates as well as rates of certain reaction steps under the measurement conditions can appear substantially lower than the sensitivity threshold of the instrumental techniques applied. In this case, the information gathered often inadequately reflects the chemistry behind the processes on the surface of a functioning catalyst.

Yet another problem encountered by many surface science researchers refers to the use of metal single crystals as subjects of catalysis-related studies instead of small metal particles

V I Bukhtiyarov G K Boreskov Institute of Catalysis, Siberian Branch of the Russian Academy of Sciences, prosp. Acad. Lavrentieva 5, 630090 Novosibirsk, Russian Federation. Fax (7-383) 330 80 56, tel. (7-383) 330 67 71, e-mail: vib@catalysis.nsk.su

Received 17 April 2007
Uspekhi Khimii **76** (6) 596 – 627 (2007); translated by Ya V Zubavichus

supported on an inert matrix, which represent real catalysts in most cases. Since all heterogeneous reactions proceed on the surface of a solid, the surface/volume ratio has to be increased in order to enhance the utilisation coefficient of the active metal. Therefore, metal particles in real practically applicable catalysts are often so small (3–5 nm) that deviations in their properties from those of the bulk metal have to be taken into account, which is referred to as the size effect and gives rise to the 'material gap' problem.

Starting from the end of the 1980s, these two problems were seriously addressed. In particular, high-pressure reactors and cells integratable into standard ultrahigh vacuum (UHV) equipment were designed, which enabled measurements of catalytic reaction rates at atmospheric pressures followed by an *ex situ* analysis of the catalyst composition avoiding its contact with air. Thus it became possible to systematically compare the surface composition and morphology of catalysts before and after the reaction with the respective changes in the catalytic activity. Such a combined *ex situ* approach was applied by Over *et al.*[5–7] to address the 'pressure gap' problem in the case of CO oxidation on the Ru(0001) surface. By using temperature-programmed desorption (TPD), scanning tunneling microscopy (STM), LEED and XPS, they demonstrated that the clean Ru(0001) surface, which is inert under UHV conditions, is oxidised to RuO_x under the action of the reaction medium. The latter proved to be even more reactive with respect to the CO oxidation than platinum, which is a prototypical catalyst for this reaction. Such an oxidised surface cannot to be formed spontaneously under UHV conditions. Another example of the efficiency of this approach to the studies of model catalytic systems was demonstrated by Campbell *et al.*[8–10] for the oxygen and ethylene adsorption on single-crystalline (111) and (110) faces of silver. In this study, a special design of the electron spectrometer was used, which made it possible to transfer samples from a high-pressure microreactor to an UHV analytical chamber for the characterisation of the preprocessed surfaces with various instrumental techniques very fast (in less than 20 s). Still, such experiments are not free form the major drawback of the post-reaction analysis: evacuation of the reaction medium effectively eliminates weakly bound adsorbed species that could act as key species governing the catalyst reactivity under the reaction conditions.

A different in principle approach to address the 'pressure gap' problem was utilised by the British company 'Vacuum Generators', which is a recognised world-leading manufacturer of UHV equipment. This company designed and put into production a 'high-pressure' electron spectrometer,† which enabled the *in situ* registration of photoelectron spectra at pressures of up to 1 mbar,[11] *i.e.*, 6 orders of magnitude higher than in serial spectrometers. With such spectrometers that operate at pressures close to that of typical catalytic reactions, the quantitative determination of the relationships between the composition of the surface layer of a sample and its catalytic performance became possible. It is apparent that this approach to the solution of the 'pressure gap' problem is very promising.

The necessity to address the size effects within the context of the 'material gap' problem became apparent in the end of the 20th century, when studies of catalytic properties of supported metal catalysts as a function of the size of the active component (see Refs 14, 15 and references therein) revealed that the rates of many catalytic reactions normalised to the number of surface atoms vary upon changes in the size of supported metal particles. Boudart[14] introduced the term structure-sensitive reactions to designate this phenomenon and distinguish it from structure-insensitive reactions, the rates of which were independent of the size of catalytic metal particles. Interestingly, the size effect can be both positive (*i.e.*, the reaction rate increases with a decrease in the size of supported metal particles) and negative (*i.e.*, the reaction rate decreases). It was size effects that encouraged extensive investigations into the electronic, structural and adsorption properties of small metal clusters in comparison with those of bulk metals.

However, only low efficiency and slow progress in this field were achieved with traditional supported catalysts. Indeed, real catalysts that are usually prepared by impregnation of a support with a large specific surface area with aqueous solutions of salts of the active component followed by the drying and reduction of the salt to the metal state refer to colloidal systems. The collection of fully reproducible data on such systems is naturally very difficult. This fact together with possible contamination of the catalytic systems by undesired admixtures either coming from the substrate material or introduced at the steps of catalyst synthesis likely explain the large contradiction in data on catalytic activities of nominally identical catalytic systems reported by different authors.[15] Poor reproducibility of the results can be overcome if the synthesis of supported catalysts and their subsequent characterisation are repeated many times. Furthermore, it has to be taken into account that the preparation of a series of catalysts with a systematically varying mean size of metal particles is a time-consuming procedure by itself.

As an alternative, model supported catalysts can be prepared in a reproducible way by vacuum deposition of disperse metal particles onto the surface of a planar substrate. Thin oxide films grown on the surface of metal single crystals or surfaces of oxide single crystals can be used as the substrates.[16,17] Indeed, the preparation of metal nanoparticles directly in a UHV spectrometer makes it possible, first, to carefully pre-clean the substrate and deposition system and, second, to transfer the sample into an analytical chamber without its contact with air. This preparation scheme avoids introduction of undesired contaminants and enables quick production of series of samples with variable sizes of metal clusters. This way of the simulation of real catalysts is widely applied to the analysis of the electronic properties and morphology of metal nanoparticles as a function of their size (for example, see Refs. 16–20). Several attempts have been undertaken to study the specificity of adsorption on disperse metal particles.[18–21] It is of note that the inconcistency between the model and real substrates intrinsic to the preparation method has not only negative, but also positive aspects, since it allows a wider choice of the substrate material. For instance, an oxide substrate can be replaced by a carbon-based one. This makes it possible to appeal to supplementary instrumental techniques to probe the adsorption properties of metal clusters. With graphite substrates instead of oxide ones, XPS can be efficiently applied to study the oxygen adsorption on metal clusters since in this case relatively weak O1s signal from the adsorbate is not superimposed on the prevailing background singal from Al_2O_3 or SiO_2 substrates. And thus adsorbed oxygen species can be identified based on an analysis of the O1s spectra.

The low specific surface area of single crystals prevents measurements of the specific catalytic activity of single crystal-based model systems in many catalytic reactions. Nevertheless, the chemistry underlying the catalytic action of metals cannot be understood without comparison of the results on model objects with the catalytic properties of real catalysts. Investigations into the reactivity of small clusters towards the reactants and reaction products, necessarily as a function of their size, can help to fill the gap between surface science studies and the real catalysis.

Therefore, the nature of the catalytic action of metals can efficiently be analysed using an approach depicted schemati-

† Two such spectrometers were purchased by Cardiff University (UK)[12] and G K Boreskov Institute of Catalysis (Novosibirsk, Russia).[13]

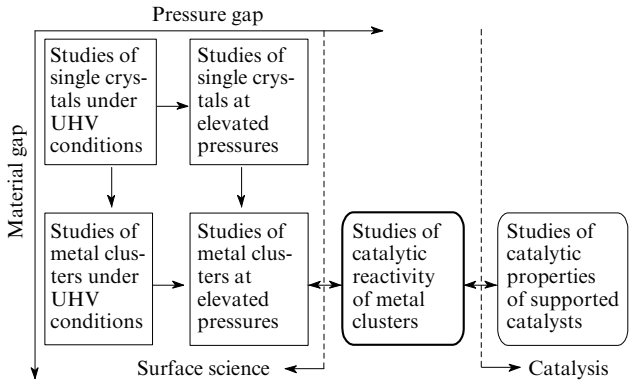


Figure 1. A scheme of the suggested approach aimed at establishing the structure – activity relationship in heterogeneous catalysts.

cally in Fig. 1. A study should start with well-ordered single crystals under UHV conditions and then move along both increasing the pressure of the reaction medium (*i.e.*, from left to right) and complicating the object under study (*i.e.*, from top to bottom). The movement from left to right implies the elimination of the 'pressure gap' problem, whereas that from top to bottom addresses the 'material gap' problem. Finally, instrumental techniques for surface studies have to be applied to elucidate the structure of the active sites in real catalysts during their formation, activation and deactivation and these data are to be compared to the results of model studies.

It is evident that in order to retrieve reliable data on the structure of functioning catalysts, not only ITSS but also bulk-sensitive techniques, such as transmission electron microscopy (TEM), X-ray diffraction and X-ray absorption methods (EXAFS, XANES), have to be applied.

Examples of studies accomplished over recent years in the Laboratory of surface science of the G K Boreskov Institute of Catalysis as well as in other world-renowned research centres specialised in the field, which are described in detail below, demonstrate that the above approach conforms with the modern trends in surface science as applied to catalysis by helping to establish the structure – activity relationship in heterogeneous catalysts and advancing towards purposeful design of highly active, selective and deactivation-resistant catalysts.

It has to be however noted that several methodological problems non-typical of traditional surface science, which hinder the retrieval of required information, emerge in the implementation of this approach in practice. Possible solutions of these problems are often highly specific and cannot be generalised and standardised. With this regard, in the description of experimental results below, we shall put an emphasis (somewhat greater than in traditional reviews) on relevant technical details of the respective measurements.

II. The 'pressure gap' problem

As has been stated in the Introduction, the development or optimisation of surface science techniques capable of *in situ* monitoring of processes directly in the course of a chemical reaction represents the most promising way to address the 'pressure gap' problem.[22–38] Among techniques working at pressures close to those of real catalytic reactions ($P > 0.1$ mbar), Infrared Reflection-Absorption Spectroscopy (IRAS),[22–24] in particular, in the polarisation modulation mode, Sum-Frequency Generation (SFG) spectroscopy,[25–28] X-ray Absorption Near-Edge Structure (XANES),[29–31] X-ray Photoelectron Spectroscopy (XPS)[11–13,32–36] and scanning tunneling microscopy[37,38] are of special note.

X-Ray photoelectron spectroscopy occupies a special place in this list being one of the best analytical techniques for studies of the chemical composition and electronic structure of solid surfaces. The physical limit of pressure at which an XPS spectrum can still be measured is determined by the photoelectron mean-free path. The latter value is of the order of a few millimetres at a pressure of 1 mbar. Meanwhile, the typical pressure in the vast majority of XPS spectrometers is $\sim 10^{-9}$ mbar, which required for the safe operation of an X-ray source, an electron energy analyser and a secondary electron multiplier. Due to fundamental difficulties in combining these two requirements in one spectrometer design, the *in situ* mode of XPS data collection had been inaccessible for a long time. The situation has changed only recently and there are currently several research groups worldwide running XPS spectrometers capable of measuring spectra at a pressure range from 10^{-9} mbar to 1 mbar.[11–13,32–36] One of such dedicated high-pressure machines manufactured by 'Vacuum Generators' is installed at the Boreskov Institute of Catalysis in Novosibirsk. Its preliminary adaptation to the *in situ* studies of catalytic reactions at pressures of up to 10^{-2} mbar was accomplished in the Laboratory of metal catalysts.[13] The additional cycle of spectrometer optimisation enabled the extension of the operational pressure range to 0.2 – 0.3 mbar (Refs 34 – 36). This value is only severalfold lower than the maximum achievable operational pressure realised in advanced spectrometers installed at the synchrotron radiation beamlines‡ in ALS (Berkeley, USA)[33] and BESSY (Berlin, Germany).[35]

A few illustrative examples of the application of XPS in the *in situ* mode to the elucidation of mechanisms of catalytic reactions are given below.

1. Interaction of CO with the Pd surface

As the first example, let us consider the combined application of XPS and SFG to the elucidation of interactions of CO and CH_3OH with the palladium surface in a wide range of temperatures and pressures. Simultaneous utilisation of several complementary instrumental techniques, which increases the reliability of conclusions derived from the experimental results, reflects one of the trends in contemporary surface science. Sum-frequency generation spectroscopy based on the irradiation of a sample surface with two pulse lasers operated in visible and IR spectral ranges is a rather complicated but still very promising non-linear optical technique suitable for the *in situ* studies of adsorbed complexes. The physical background of this method is described in detail elsewhere.[25–28] During the measurements, the frequency of the visible-light laser is kept constant ($\lambda = 532$ nm), whilst that of the IR laser is scanned over a certain range, which gives rise to the appearance of characteristic SFG resonances under specific conditions associated with the vibrational excitations of adsorbed molecules.[25,26] The SFG is a second-order non-linear optical process, which has a non-vanishing probability exclusively in a non-centrosymmetrical medium. The requirement of the absence of the local inversion symmetry is always met for an interface and, as a rule, violated for an isotropic gas and the bulk of a solid, which provides the ultimate surface sensitivity of this method. According to the selection rules, both IR- and Raman-active vibrations are manifested in the SFG spectra. With SFG, vibrational spectra of adsorbed species can be collected in the *in situ* mode at high pressures up to the

‡ The extreme brilliance of synchrotron radiation makes it possible to approach to the theoretical limit of pressures in the *in situ* experiments (1 – 2 mbar).

atmospheric pressure, which is an evident advantage of this technique.

On the other hand, XPS provides direct quantitative information on chemical composition of the adsorbed and near-surface layers of the catalyst under study and its variation under high pressures (*vide supra*).

The mechanism of activation of the C–O bonds on the surfaces of transition metals attracts keen attention from specialists working in the field of heterogeneous catalysis. It plays a key role in the carbon monoxide hydrogenation as well as methanol oxidation and dehydrogenation, which are the important steps of large-scale industrial processes of production of hydrocarbons, aldehydes, alcohols and hydrogen.[39–44] In particular, the C–O bond activation (followed by its cleavage) is a necessary step in the synthesis of hydrocarbons according to the Fischer–Tropsch process. Meanwhile, the progressive carbon deposition on the catalyst surface as a result of the CO dissociation often reduces its catalytic activity due to the shielding of active surface sites. Actually, the activity and selectivity of all of the above reactions is governed by the activation of the C–O bonds depending on the catalyst nature, gaseous medium composition and reaction conditions. With this regard, deep understanding of the mechanism of the C–O activation on the surface of transition metals is a prerequisite to the prediction of the catalytic action and consequently to the purposeful design of catalysts with improved efficiencies for specific reactions.

Figure 2 shows SFG and XPS spectra measured *in situ* during the CO adsorption on atomically smooth Pd(111) single-crystalline face at 400 K. At low pressure ($P_{CO} = 10^{-6}$ mbar), the SFG spectrum reveals a single line at 1910 cm^{-1} attributable to stretching vibrations of bridge-bonded CO molecules. At the same time, a narrow symmetrical line centred at 285.6 eV emerges in the C1s XPS spectrum (Fig. 2*b*), which can thus also be ascribed to adsorbed CO molecules in bridging positions. Upon an increase in pressure, a new SFG resonance at 2075–2080 cm^{-1} appears, which is indicative of the appearance of terminally bound species due to the higher surface concentration of CO_{ads}. Meanwhile, the C1s XPS line broadens due to the emergence of a new component of terminally bound CO with $E_b = 286.3$ eV (according to the deconvolution of the spectra into the components *1′* and *1″*). Such an attribution of the C1s components agrees with the results of high-resolution XPS obtained by Surnev *et al.*,[45] who demonstrated that the three-fold hollow, bridge-bonded and on-top CO molecules on Pd(111) are characterised by similar C1s binding energies of 285.6 ± 0.1 eV, 285.85 eV and 286.3 eV, respectively. The C1s feature at around 290 eV appearing at even higher pressures $P_{CO} > 5 \times 10^{-2}$ mbar (the component *1* in Fig. 2*b*) can be assigned to gaseous carbon monoxide.[46]

SFG and XPS spectra registered *in situ* during the CO adsorption on the atomically smooth Pd(111) crystal face at 200 K and $P_{CO} = 1$ mbar (SFG) or 0.1 mbar (C1s) are shown in Fig. 3. These experimental conditions (*viz.*, high pressure and low temperature) provided the maximum possible coverage of palladium surface with CO molecules of 0.75 monolayers. The respective SFG spectrum reveals two vibrational bands at 1895 cm^{-1} and 2107 cm^{-1} assigned to three-fold and on-top species, respectively. The conlcusion on the presence of terminally coordinated CO molecules on Pd(111) is supported by the comparison of the C1s XPS spectrum measured under similar conditions with that measured at $T = 400$ K and $P_{CO} = 10^{-6}$ mbar, *i.e.* where such species are surely absent (see the SFG spectrum in Fig. 3*a*). The difference spectrum (spectrum *3* in Fig. 3*b*) obtained by subtracting the contribution of the three-fold CO species from the total C1s spectrum is characteristic of the terminal adsorbed CO species. This conclusion is supported by the quantitative estimation of relative

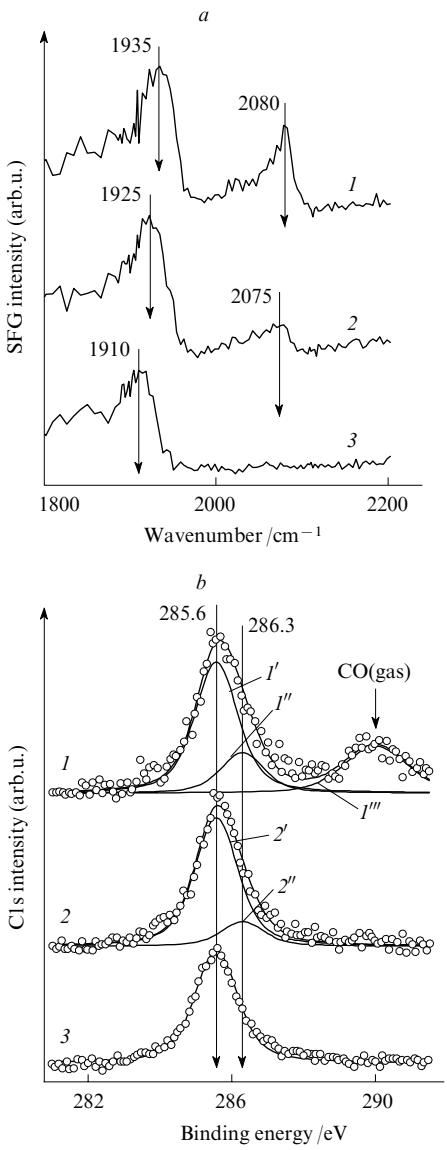


Figure 2. SFG (*a*) and C1s XPS (*b*) spectra measured *in situ* during CO adsorption on the atomically smooth Pd(111) surface at 400 K as a function of P_{CO}.
P_{CO}/mbar: (*a*) 1 (*1*), 10^{-3} (*2*), 10^{-6} (*3*); (*b*) 0.1 (*1*), 5×10^{-3} (*2*), 10^{-6} (*3*). Lines (*1–3*) are experimental data, (*1′*, *1″*) and (*2′*, *2″*) are deconvolution of the experimental curve into two components corresponding to bridge-bonded (*1′* and *2′*) and on-top (*1″* and *2″*) CO molecules; (*1‴*) is a component attributed to gaseous CO. Hereinafter, all C1s spectra are normalised to the integral intensity of the respective Pd3d lines.

surface concentrations of the three-fold (spectrum *2*) and on-top (spectrum *3*) CO_{ads}. The respective ratio of ~1.9 obtained from the experimental XPS spectra is close to the value 2 determined earlier for the (2 × 2)-3CO surface structure, which corresponds to the maximum coverage of Pd(111) with the CO molecules ($\Theta = 0.75$ monolayers). It is also of note that this clear separation of the C1s spectral component responsible for the terminally coordinated CO species ($E_b = 286.3$ eV) validates the spectral deconvolution procedure utilised in the analysis of the XPS spectra shown in Fig. 2.

The application of XPS to the *in situ* studies of the CO adsorption on Pd(111) helped to answer the important question whether the dissociation of C–O bonds can proceed on palladium. In a number of earlier publications (for instance, see Refs 47–50), a dissociative character of the CO adsorption

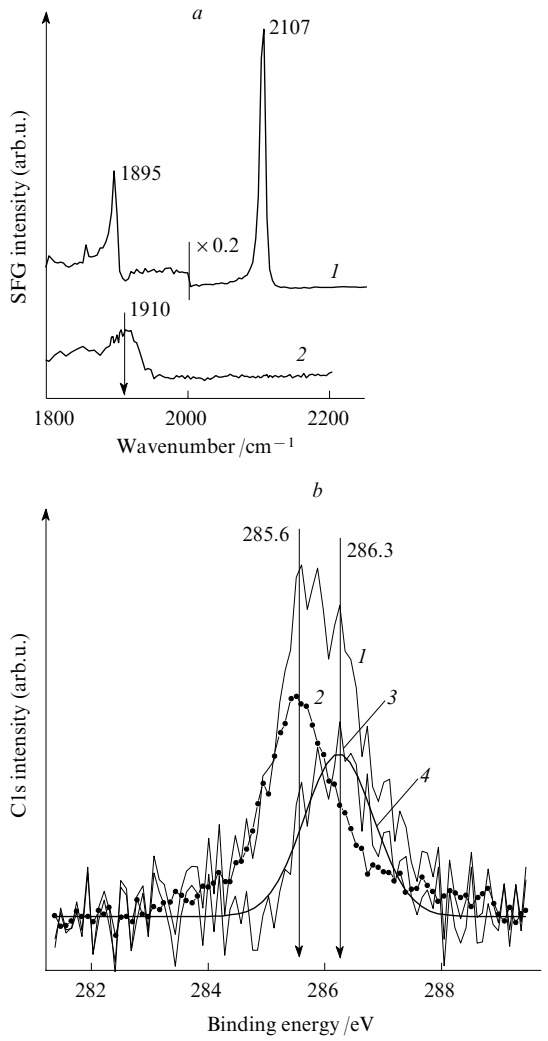


Figure 3. SFG (*a*) and C1s XPS (*b*) spectra measured *in situ* during CO adsorption on the atomically smooth Pd(111) surface at 200 K and 1 mbar (curve *1*) and at 400 K and 10^{-6} mbar (curve *2*).
The curve (*3*) is calculated by the direct subtraction of the respective C1s spectra, (*4*) is the averaged spectrum (*3*).

on the surface of highly disperse palladium particles was suggested. On the other hand, no CO dissociation was observed in other studies,[51–53] despite the detection of weakly bound adsorbed CO species on palladium particles with a size of 2–3 nm. A strong influence of pressure on the adsorption process can be a reason for this apparent discrepancy. The rate of the CO disproportionation under UHV conditions is quite low, such that very often no respective products can be detected. Indeed, the probability of CO dissociation on the palladium surface is very low according to theoretical calculations.[53–55] However, the combined application of SFG and XPS decisively rules out this explanation since only lines of molecularly adsorbed CO are observed in all the C1s XPS spectra, including those measured *in situ* at pressures of up to 1 mbar.[46] In the cases of CO dissociation or formation of carbonyl structures [*e.g.*, $Pd(CO)_2$], the appearance of additional photoemission components at about 284 eV and 287 eV, respectively, is expected.[56,57] Thus, no indication of the CO dissociation or the formation of other adsorbed species on the Pd(111) surface was found by *in situ* measurements over the pressure range from 10^{-6} mbar to 1 mbar and temperature range from 200 K to 400 K.

2. Interaction of CH_3OH with the Pd surface

Despite the fact that the interaction of methanol with the palladium surface has been the subject of intense investigations by many research groups for a long time, the mechanism of catalytic methanol decomposition remains disputable.[58–70] The majority of specialists have a consensus that it is the dehydrogenation of methanol to CO and H_2 that is the predominant pathway of this reaction.[58–62] As has been established,[58] at low temperature, methanol is adsorbed on the palladium surface molecularly through the oxygen lone pair. A layer of adsorbed methanol and formaldehyde molecules as well as methoxy groups is formed following methanol adsorption at 170 K.[59,60] An investigation into the decomposition of methanol on Pd(111) by means of Secondary-Ion Mass Spectrometry (SIMS)[61] and EELS[62] revealed that the cleavage of the O–H bond in an adsorbed methanol molecule occurs as the first step of the reaction to yield the CH_3O groups, which further decompose to CO and H_2 by the stepwise detachment of the hydrogen atoms upon heating. The reaction proceeds *via* CH_2O and CHO. Such a mechanism is supported by the TPD and EELS data.[59,60]

Nevertheless, some authors believe that the methanol decomposition on Pd(111) accurs as the C–O bond cleavage to yield adsorbed CH_x ($x = 0-3$) species.[54,63–65] The probable dissociation of the C–O bond in a methanol molecule upon its adsorption on the Pd(111) surface has been suggested by Winograd *et al.*[54,63] based on the XPS, SIMS and TPD data. Species $CH_{3,\,ads}$ were detected on Pd(111) (in a concentration of $\Theta = 0.04$ monolayers) after methanol adsorption at 110 K (to $\Theta \approx 0.5$ monolayers) followed by annealing *in vacuo* at 175 K. Further annealing resulted in the dehydrogenation of the CH_3 species to $CH_{2,\,ads}$, CH_{ads} and C_{ads}.

Notwithstanding, no cleavage of the C–O bond in methanol molecules upon adsorption on Pd(111) was detected in a TPD study of isotopically labelled compounds $^{13}CH_3{}^{16}OH$ and $^{12}CH_3{}^{18}OH$ over a wide temperature range (87–265 K), which provided a very high sensitivity of $\sim$0.01 monolayers.[64] It was suggested that this apparent discrepancy is due to different rates of competing pathways of the methanol decomposition on the palladium surface. For instance, the rate of methanol dehydrogenation to CO is approximately two orders of magnitude higher than the decomposition through the C–O bond cleavage,[66] and thus it is nearly impossible to detect the formation of $CH_{x,\,ads}$ species under UHV conditions at low temperatures and small methanol exposures.

This hypothesis was verified in a combined XPS and SFG study of the methanol interaction with the atomically smooth Pd(111) surface at variable temperatures and pressures.[67,68] The SFG (*a*) and C1s XPS (*b*) spectra measured *in situ* during the methanol decomposition on Pd(111) is shown in Fig. 4. The methanol adsorption at room temperature and 10^{-6} mbar gives rise to the emergence of a vibrational SFG resonance at 1915 cm^{-1} corresponding to bridging adsorbed CO molecules at a coverage of $\Theta \approx 0.5$ monolayers.[27,28,45,46,69] Meanwhile, the C1s XPS spectra reveal two components with binding energies of 284 eV and 285.6 eV, which can be assigned to hydrocarbon $CH_{x,\,ads}$ ($x = 0-3$) and oxygen-containing CH_xO_{ads} ($x = 0-3$) species based on an analysis of the literature data.[45,46,56] Quantitative agreement between the coverages ($\Theta \approx 0.5$ monolayers) estimated from the relative intensity of the C1s line at $E_b = 285.6$ eV and from the SFG data allowed the authors to limit the range of potential species and assign the C1s component with $E_b = 285.6$ eV to adsorbed CO.[67] This assignment is supported by numerous studies indicating that the decomposition of the CH_3O groups to CO_{ads} on palladium proceeds efficiently already at 200–250 K.[60,62,70] With an increase in residence time, the intensity of the XPS signal at 284 eV progressively increases, whereas that of the component at 285.6 eV remains virtually constant.

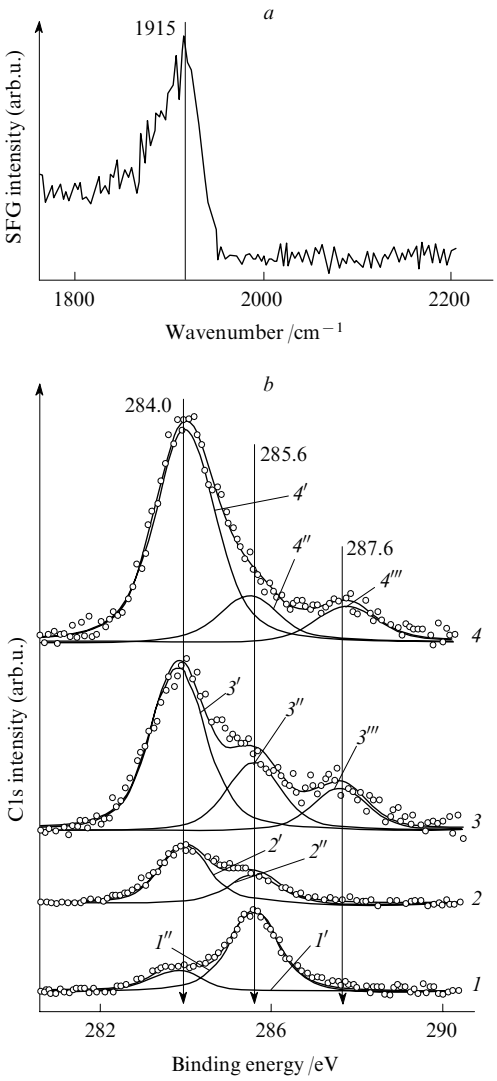


Figure 4. SFG (*a*) and C1s XPS (*b*) spectra measured *in situ* during the methanol decomposition on the atomically smooth Pd(111) surface. (*1*) $P = 10^{-6}$ mbar and $T = 300$ K; (*2*) $P = 10^{-6}$ mbar and $T = 400$ K; (*3*) $P = 0.1$ mbar and $T = 300$ K; (*4*) $P = 0.1$ mbar and $T = 400$ K. The SFG spectrum was registered at 300 K and a methanol pressure of 10^{-6} mbar. The experimental C1s spectra (curves *1*–*4*) and their deconvolution into components (*1′*, *1″*, *2′*, *2″*, *3′*, *3″*, *3‴*) and (*4′*, *4″*, *4‴*) are shown.

An increase in temperature up to 400 K or in the methanol pressure up to 0.1 mbar results in an abrupt increase in the surface concentration of the CH_x species (see Fig. 4*b*). In particular, the absolute intensity of the C1s component with $E_b = 283.8$ eV corresponds to $\Theta \approx 1.0$ monolayer at 300 K and $P_{MeOH} = 0.1$ mbar (the spectrum *3*). Despite this large apparent coverage of the Pd(111) surface with the CH_x species, a part of the surface remains covered with adsorbed CO molecules ($\Theta \approx 0.4-0.5$ monolayers). The total concentration of adsorbed species (including both CH_x and CO) exceeding one monolayer was explained by either partial dissolution of carbon in the near-surface region of palladium [71] or formation of three-dimensional carbon structures. The amount of carbon-like species further increases at 400 K ($\Theta \approx 1.5$ monolayers), which is accompanied by a small shift of the respective line towards higher binding energies ($E_b = 284.0$ eV). This change probably reflects some chemical transformations of the carbon particles.

These results clearly demonstrate that the C–O bond of the methanol molecule is activated on the atomically smooth Pd(111) surface at a measurable rate even at 300–400 K. The methanol decomposition rate and the amount of deposited carbon increases with an increase in methanol pressure. Carbon particles formed as the methanol decomposition product lead to the progressive coking of the metal surface and ultimately to its complete deactivation. Due to this process, no products of the catalytic methanol decomposition on Pd(111) (*i.e.*, CO and H_2) were detected by means of gas chromatography at elevated pressures (15–30 mbar of methanol in a helium atmosphere) and temperatures (300–600 K) even after their accumulation for several hours.[68] On the other hand, the introduction of oxygen into the reaction mixture immediately resulted in the appearance of the methanol total oxidation products, *viz.*, CO_2 and H_2O.

Based on these experimental results, the following scheme of the methanol interaction with the Pd(111) surface can be proposed. The first step of the decomposition is cleavage of the O–H bond to yield the methoxy groups.[59, 60, 62, 64] The adsorbed methoxy groups as well as methanol molecules are bound to the palladium surface through the oxygen lone pairs. They are oriented nearly perpendicular to the surface.[62] As the dehydrogenation proceeds, the molecular axis of the adsorbed complex is rotated by 90°, such that formaldehyde molecules (CH_2O_{ads}) and formyl groups (CHO_{ads}) are oriented parallel to the palladium surface.[65, 66] The final dehydrogenation product, CO, is oriented again perpendicular to the surface but it is bound to the metal atoms through the carbon atom.[72, 73]

The formation of carbon deposits on the atomically smooth Pd(111) surface observed experimentally [67, 68] supports the activation mechanism of the C–O bonds upon the methanol interaction with the palladium surface schematically depicted in Fig. 5. It is evident that an increase in the lifetime of the reaction intermediates should give rise to a higher probability of the C–O bond dissociation. Likely, this is a reason for the experimentally observed increase in the rate of carbon accumulation on the Pd(111) surface at high reaction pressures

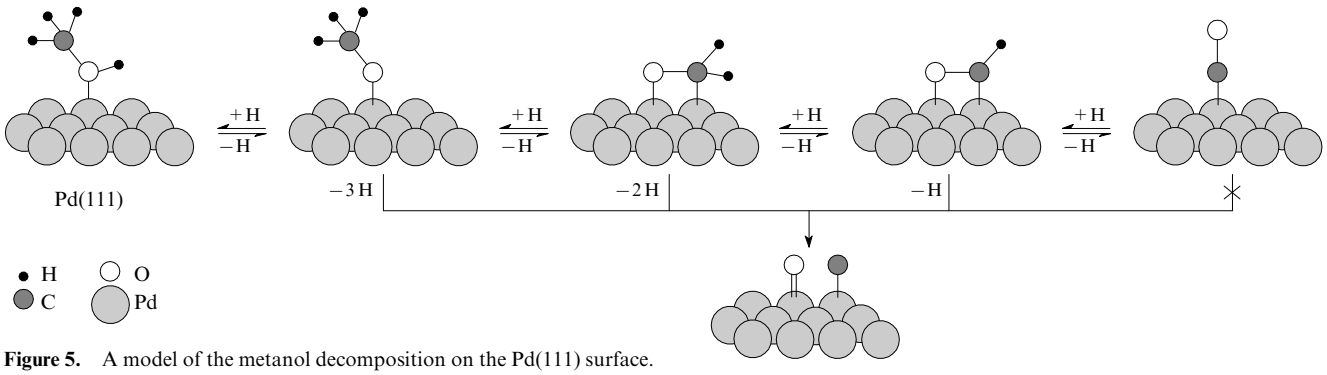


Figure 5. A model of the metanol decomposition on the Pd(111) surface.

(see Fig. 4) and in the presence of defects on the surface of supported palladium clusters.[66]

Taking into account the principle of microscopic reversibility of reaction steps, it might be assumed that the CO hydrogenation on palladium

$$CO + 2H_2 \longrightarrow CH_3OH$$

can also be accompanied by the C—O bond dissociation and catalyst deactivation due to the accumulation of carbon deposits. The emergence of the respective C1s signal with ($E_b \approx 284$ eV) was indeed detected in the XPS spectra measured *in situ* during the interaction of CO + H_2 mixtures with Pd(111) surfaces.[74]

All these results are well explained within the Blyholder model, which describes the interaction of CO with transition metal surfaces as an electron density exchange between the metal d orbitals and 5σ/2π* molecular orbitals of CO. Presumably, the geometry of the adsorption complex is the key factor governing this interaction, especially, the electron back donation from the metal d orbitals to the 2π*-antibonding molecular orbitals of CO. In the case of an adsorbed CO molecule, the orientation perpendicular to the palladium surface suppresses the back donation contribution and thus provides the inertness of palladium towards the C—O bond dissociation. The formation of intermediates like CH_xO ($x = 1-3$) in the course of the methanol dehydrogenation (or CO hydrogenation) promotes the electron transfer from the metal to the 2π*-antibonding orbital of CO, which weakens the C—O bond and ultimately gives rise to its dissociation and formation of carbon deposits on the palladium surface.

3. Ethylene epoxidation over silver

It has to be stressed that the collection of spectral data in the presence of a reaction medium over the sample (at $P = 0.1-1$ mbar) in the *in situ* mode does not *a priori* provides information on the mechanism of catalytic reactions. Indeed, adsorbed species detected on the surface of a catalyst at high pressure are not necessarily catalytically active species or reaction intermediates. This issue can be effectively solved by combining the studies of the state of a catalyst surface with measurements of its catalytic properties (such as activity and selectivity) by means of mass spectrometry or gas chromatography. The efficiency of such an approach is demonstrated below by the example of a combined study of the ethylene epoxidation reaction on silver using mass spectrometry and a number of spectral techniques (including XPS, UPS, AES and XANES).[30,75–77]

Despite numerous studies devoted to the ethylene epoxidation on silver by diverse instrumental techniques,[8–10,12,13,78–82] a number of key questions on the mechanism of this reaction remain disputable in the literature. Recent kinetics measurements have clarified some important points, but due to the lack of direct experimental data, there are still a few issues unaddressed. In particular, neither the nature of actual oxygen species driving the epoxidation,[8–10,78–79] nor the structure of the key intermediate[78–82] yielding ethylene oxide were unambiguously established. Ethylene coordinated in a way similar to π-complexes[78–80] or an oxametallacycle[81,82] were regarded as such intermediates. This stipulates the necessity of *in situ* measurements during the reaction to establish direct quantitative correlations between the yield of ethylene oxide and surface composition. Recently, the results of a series of studies on the ethylene epoxidation on silver using XPS and Proton-Transfer Reaction Mass Spectrometry (PTR-MS) jointly conducted by specialists from the G K Boreskov Institute of Catalysis SB RAS and the Department of Inorganic Chemistry, the Fritz Haber Institute (Berlin, Germany) have been published.[75–77]

Figure 6 shows ethylene and ethylene oxide partial pressures in the reaction cell of a photoelectron spectrometer as a function of temperature and reaction duration. The final regions of the plots were measured in the flow of pure ethylene (no O_2 was supplied) at $T = 470$ K (*a*) and 520 K (*b*), respectively. The partial pressure values were calculated from the respective PTR-MS signals corresponding to $m/z = 45$. The ionisation of gaseous species for the subsequent separation in a mass analyser in this relatively uncommon variant of mass spectrometry, was achieved through the proton transfer from H_3O^+ ions generated in a special source to the molecules subject to analysis. The reaction

$$S + H_3O^+ = SH^+ + H_2O,$$

where S is the substrate, yields a molecular ion SH^+ with a mass larger (due to a surplus proton) than that registered by traditional mass spectrometry by 1 a.m.u.. This specific ionisation mechanism guarantees that only substances with proton affinities higher than that of hydroxonium ions (*e.g.*, ethylene oxide but not CO_2) contribute to the mass spectra. Furthermore, this ionisation method virtually completely avoids the fragmentation of the molecular ion into lower-molecular-mass fragments, which greatly facilitates quantitative analysis of the experimental data. The high sensitivity of PTR-MS technique to organic molecules, such as ethylene oxide, is yet another its advantage. A detailed description of this modification of mass spectrometry can be found elsewhere.[83]

The PTR-MS data presented in Fig. 6*a* indicate that the signal of ethylene oxide is negligible at $\leqslant 370$ K but is reliably detected at $T = 420$ K. Further increase in temperature results in an abrupt increase in the ethylene oxide partial pressure, whereas a slow but continuous decrease in the partial pressure of C_2H_4O starts above $T \geqslant 470$ K, which is explained by the deactivation of the catalyst at these temperatures. After stop of

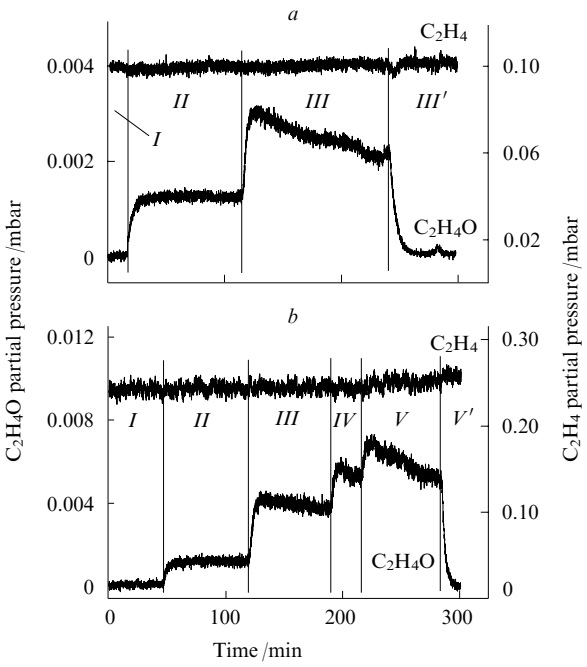


Figure 6. Changes in partial pressures of ethylene oxide and ethylene at $P_{C_2H_4} = 0.1$ (*a*) and $P_{C_2H_4} = 0.24$ mbar (*b*) (the oxygen pressure is 0.25 mbar in both cases) as a function of temperature.
T/K: 370 (*I*), 420 (*II*), 470 (*III*), 500 (*IV*), 520 (*V*). The last regions of the spectra (regions *III*′ and *V*′) were collected after cessation of the oxygen supply. The partial pressures were recalculated from ion currents measured by mass spectrometry (see text).

the oxygen flow, the PTR-MS signal of ethylene oxide rapidly drops down to the background value. These results imply that ethylene oxide forms as a product of the direct catalytic ethylene oxidation on silver at a pressure in the range of 0.1–0.5 mbar, and the epoxidation rate increases with an increase in temperature. This conlcusion is supported by test measurements, which showed that no ethylene oxide is formed upon heating of ethylene in the temperature range of 300–600 K in the absence of silver. In order to analyse the composition of adsorbed layers, full sets of XPS spectra were collected in the regions of constant temperatures (see Fig. 6).[77]

The respective O1s and C1s XPS spectra measured *in situ* at $P_{C_2H_4} = 0.1$ mbar and $P_{O_2} = 0.25$ mbar are plotted in Fig. 7. All O1s spectra are normalised to the integral intensity of the

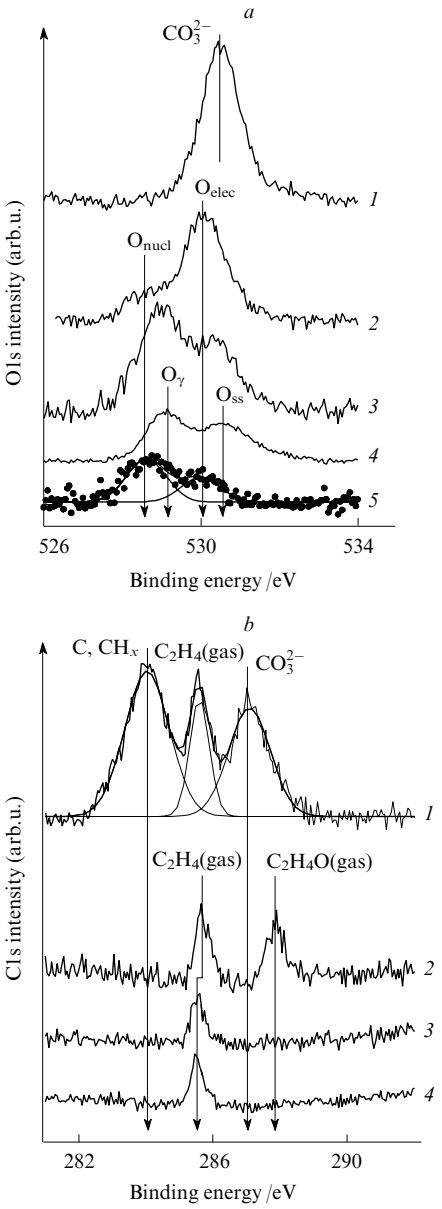


Figure 7. O1s (*a*) and C1s (*b*) XPS spectra measured *in situ* in $C_2H_4 + O_2$ reaction mixtures at $P_{C_2H_4} = 0.1$ mbar and $P_{O_2} = 0.25$ mbar as a function of temperature.
T/K: 370 (*1*), 420 (*2*), 470 (*3*). The spectrum *4* was measured at 470 K in a flow of pure ethylene after cessation of the O_2 supply. The difference O1s spectrum (curve *5* and its components) exhibit only signals of species present on the Ag surface under reaction conditions.

$Ag3d_{5/2}$ spectra. At 370 K, the XPS spectra reveal only one O1s component with $E_b = 530.5$ eV and three types of carbon-containing species corresponging to the C1s components with $E_b = 284.2$ eV, 285.8 eV and 287.3 eV, respectively (spectra *1* in Figs 7 *a* and *b*). The spectra change dramatically upon heating of the sample to 420 K: the dominant component in the O1s spectrum shifts to 530.0 eV and a shoulder appears at 528.5 eV. Meanwhile, two components with $E_b = 285.8$ eV and 287.9 eV (spectra *2* in Figs 7 *a* and *b*) are observed in the C1s spectrum. Upon further increase in temperature 470 K, the shape of the O1s signal becomes more complicated, which implies the emergence of additional components from other types of oxygen-containing species (spectrum *3* in Fig. 7 *a*). After removal of oxygen from the gas mixture, two components with $E_b = 529.1$ eV and 530.6 eV appear in the O1s spectrum (spectrum *4* in Fig. 7 *a*). The difference spectrum (spectrum *5* in Fig. 7 *a*) indicates that two O1s peaks with $E_b = 530.0$ eV and 528.5 eV present in the spectra under reaction conditions at a lower temperature disappear. In the C1s spectrum measured in a flow of pure ethylene (spectrum *4* in Fig. 7 *b*), a single peak at 285.8 eV is revealed.

It has to be noted that the large number of spectral components and the resultant ambiguities in their assignment is a common problem of the interpretation of spectra registred *in situ*. This problem can be solved by making use of supplementary reference data from traditional adsorption experiments, which in some cases requires additional measurements on special model systems. The ethylene epoxidation reaction clearly demonstrates why this supplementrary information is needed.

Indeed, despite the apparent complexity of the pattern of temperature changes in the XPS spectra, numerous experimental data available in the literature[8–10,78–81,84–86] make it possible to quite reliably assign the components observed in the XPS spectra to different surface and gaseous species. The XPS signals coming from gas molecules, which start to make appreciable contribution at $P > 0.05$ mbar,[33–36] can be differentiated from those of adsorbed species by their significantly smaller FWHM (full width at the half maximum). It is for this reason, as well as taking into account possible compositions of the mixture under the catalytic reaction, that the components with $E_b = 285.7$ eV and 287.9 eV observed in the C1s spectrum (spectrum *2*) were attributed to gaseous ethylene and ethylene oxide, respectively.[77] Indeed, rather similar binding energies of free ethylene and ethylene oxide ($\Delta E_b \approx 2$ eV) were reported earlier by Siegbahn *et al.*[85] This assignment is additionally supported by the spectral changes following cessation of the oxygen supply. The signal of gaseous ethylene ($E_b = 285.8$ eV) remains virtually unaffected, whereas that of ethylene oxide rapidly drops down to the background value (spectrum *4* in Fig. 7 *b*), which is in keeping with the disappearance absence of one of the reactants. The direct observation of gaseous ethylene oxide in the XPS spectra is a significant merit of the *in situ* measurements, since it solidly confirms the assignment of the PTR-MS signal with $m/z = 45$ to ethylene oxide rather than its isomer, acetaldehyde, which was reported by some authors.[8–10,12,13]

Other signals in the C1s and O1s spectra (see Fig. 7) were assigned to adsorbed species.[77] Temperature ranges of their existence can be used as a supplementary criterion for their assignment. In particular, the peaks at ~530.5 eV (O1s) and ~287.5 eV (C1s) observed at $T = 370$ K were attributed to surface carbonates $CO_{3,ads}^{2-}$ not only based on the binding energy values, but also taking into account that they disappear upon heating to 420 K.§ Furthermore, the atomic ratio

§ Carbonate anions adsorbed on silver are known to be stable only below 420 K.[13,78,84]

O : C = 2.8 – 2.9 calculated from the absolute intensities of the respective components corresponds to the stoichiometric value expected for carbonates (3.0). The low-binding energy peak observed in the C1s spectrum measured at 370 K (E_b = 284.2 eV) was attributed to carbon deposits (elementary carbon or hydrocarbon residues), which can accumulate on the silver surface at moderately low temperatures. It was concluded [77] that the screening of the silver surface with carbon deposits and adsorbed carbonate groups is primarily responsibly for the lack of catalytic activity of silver below 370 K (see Fig. 6).

The O1s signals observed in the XPS spectra measured at $T > 370$ K were assigned to atomic oxygen, taking into account the absence of any Cs1 signal from adsorbed carbon species. The attribution of lines with E_b = 528.5 eV and 530.0 eV to the nucleophilic and electrophilic forms of adsorbed oxygen was made on the basis of earlier publications devoted to the studies of surface interactions of polycrystalline silver foil with reaction media.[75, 76, 79] The line with $E_b \approx 529.0$ eV was ascribed to the so-called O_γ form, which has been elucidated in detail by Schlögl *et al.*[86, 87] within the context of partial methanol oxidation over silver. This species was formulated as a strongly bound atomic oxygen substituting the silver atoms in the fcc lattice. An additional O1s signal that emerges at $T > 470$ K was attributed to the near-surface oxygen O_{ss} (or O_β)¶ incorporated into the octahedral cavities of the silver fcc lattice near the surface. The subsurface location of the O_γ and O_β oxygen species explains their inertness towards ethylene. It is these forms of oxygen that remain on the silver surface after the oxygen supply is stopped. In contrast, the nucleophilic (O_{nucl}) and electrophilic (O_{elec}) oxygen species (see the difference spectrum *5* in Fig. 7 *a*) rapidly disappear from the silver surface in the absence of O_2 in the reaction mixture, which clearly indicates their high reactivity towards the ethylene oxidation.

To clarify the roles played by the nucleophilic and electrophilic oxygen species in the ethylene oxidation reaction, a quantitative comparison of the XPS and PTR-MS data collected at variable $C_2H_4 : O_2$ ratios in the gaseous reaction mixture has been carried out. The absolute intensities of the respective peaks normalised to that of the $Ag3d_{5/2}$ line were used as measures of the surface concentrations of these species. This procedure was necessary to account for the decrease in the XPS absolute line intensities for different compositions and pressures of the gas phase. The partial pressure of ethylene oxide was taking as a measure of the reaction yield. The ethylene oxide yield is correlated with the relative amounts of the nucleophilic and electrophilic oxygen species (Fig. 8). A dependence of the ethylene oxide yield on the concentration of the electrophilic oxygen is apparent: the larger the $O1s/Ag3d_{5/2}$ ratio for the component with E_b(O1s) = 530.0 eV, the higher the partial pressure of C_2H_4O. This dependence can readily be approximated by a straight line passing through the point of origin. This correlation clearly proves the involvement of the electrophilic form of the adsorbed oxygen in the ethylene oxide formation, which supports the epoxidation mechanism proposed by Bukhtiyarov *et al.*[79]

$$O_{elec} + C_2H_{4,ads} \longrightarrow C_2H_4O.$$

Note that the linear dependence of the ethylene oxide yield on the surface concentration of the electrophilic oxygen species was also observed at other temperatures (470 K and 520 K),[77] the slopes of the respective lines being increased for higher temperatures. These slopes were used to calculate the activation energy of the epoxidation reaction, which appeared in excellent agreement with the known E_{act} values measured for the epoxidation reaction over real $Ag/\alpha\text{-}Al_2O_3$ catalysts.[8–10, 78, 82] Even a decrease in the E_{act} value from 14 kcal mol^{-1} to 11.3 kcal mol^{-1} with an increase in temperature from 450 K to 500 K is reproduced.[77, 82]

¶ This form of oxygen is referred to as O_β, according to the classification adopted in earlier publications.[86, 87]

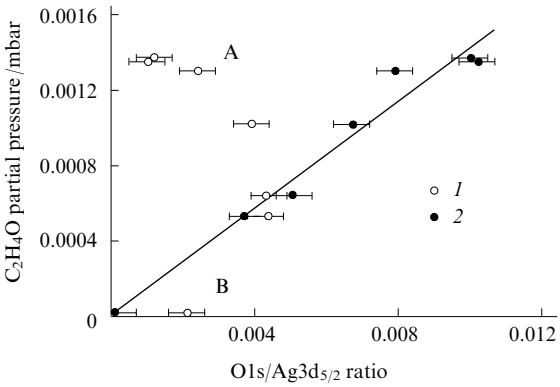


Figure 8. The yield of ethylene oxide as a function of surface concentrations of the nucleophilic (*1*) and electrophilic (*2*) oxygen species.[77] The measurements were performed at T = 420 K and varialbe partial pressures of oxygen and ethylene.

The surface concentration of the nucleophilic oxygen species correlates with the ethylene oxide yield in a more complex way (see Fig. 8). As has been found, in different experiments silver can demonstrate dramatically different catalytic activities at nearly identical surface concentrations of the nucleophilic oxygen. In particular, for $I(O1s)/I(Ag3d_{5/2}) \approx 0.02$ the partial pressure of ethylene oxide is 0.0013 mbar (which is still a reliably measured value) in one experimental point A (Fig. 8), but drops far below the detection threshold ($< 10^{-5}$ mbar) in another point B. It has to be noted that the latter case was realised at low pressure and thus the concentration of the electrophilic oxygen was negligible. If only data point in the pressure range of 0.1 – 1 mbar are taken into account, then a negative correlation of the ethylene oxide yield with the surface concentration of nucleophilic oxygen species is observed. Such a correlation can be rationalised by assuming that the nucleophilic oxygen catalyses the total ethylene oxidation. A similar conclusion was derived in earlier studies [3, 8–10, 78, 79, 88] based on the results of titration of this type of adsorbed oxygen species with ethylene. Only CO_2 and H_2O were registered as the titration products in numerous experiments. However, other authors [75, 76, 79] recognised the positive role played by the nucleophilic oxygen in the ethylene epoxidation, since it is involved in the formation of the $Ag^{\delta+}$ ions,[89, 90] which further act as adsorption sites for ethylene. According to this scheme, adsorbed ethylene then reacts with the electrophilic oxygen species to yield ethylene oxide.

The possible co-existence of two forms of oxygen atomically adsorbed on the silver surface has been substantiated for the first time by Carter and Goddard.[91, 92] Using quantum chemical calculations, they demonstrated stability of two distinct states of atomically adsorbed oxygen, *viz.*, oxide-like and oxyradical-like. The electronic structures of these forms depend on the coordination of the oxygen atom to the silver atoms. The oxyradical anion is active towards the selective alkene oxidation and is essentially equivalent to the electrophilic form of the adsorbed oxygen. The oxide oxygen, as will be shown below, can be associated with the nucleophilic oxygen form.

The specificity of chemical interactions of silver atoms with the electrophilic and nucleophilic adsorbed oxygen species were studied using X-ray Absorption Near-Edge Structure

spectroscopy (XANES, the term NEXAFS is also frequently used in the literature [75, 76]). This method provides direct information on vacant orbitals of atoms and molecules with element sensitivity. According to the dipole selection rules ($\Delta l = \pm 1$), the oxygen *K*-edge XANES spectra are formed by the electron transitions from the O1s core level to vacant oxygen p-orbitals.[93]

Figure 9 *a*,*b* shows the oxygen *K*-edge XANES spectra collected under conditions providing the selective formation of either nucleophilic (spectrum *1*) or electrophilic (spectrum *4*) oxygen species. In the case of O_{nucl}, the XANES spectrum reveals two distinct resonances at ~531 eV and ~539 eV (Fig. 9 *a*). According to the literature data,[94, 95] the presence of a narrow low-energy resonance below the main absorption edge at ~531 eV indicates the effective hybridisation between the oxygen 2p and silver 4d electrons. The broader signal just above the main absorption edge is due to the hybridisation of oxygen p and silver 5sp electrons. The presence of a narrow absorption pre-edge peak in the spectrum of O_{nucl} clearly indicates that its 2p shell is not filled completely. In fact, in the case of a purely ionic Ag—O bond, the transfer of two electrons from the silver atoms to the oxygen atom should give rise to the electronic configuration $O1s^2 2s^2 2p^6$, and the transition 1s → 2p responsible for the pre-edge peak in the XANES spectrum will be formally forbidden. With this regard, a value of the partial negative charge on the oxygen atom estimated from the Auger spectra [75, 76] (~1.65 e per oxygen atom) is in complete accordance with its nucleophilic nature, and the involvement of the silver 4d electrons into the formation of the Ag—O bonds explains its high ionicity and the observed shift of the Ag3d line by 0.5 eV.[75]

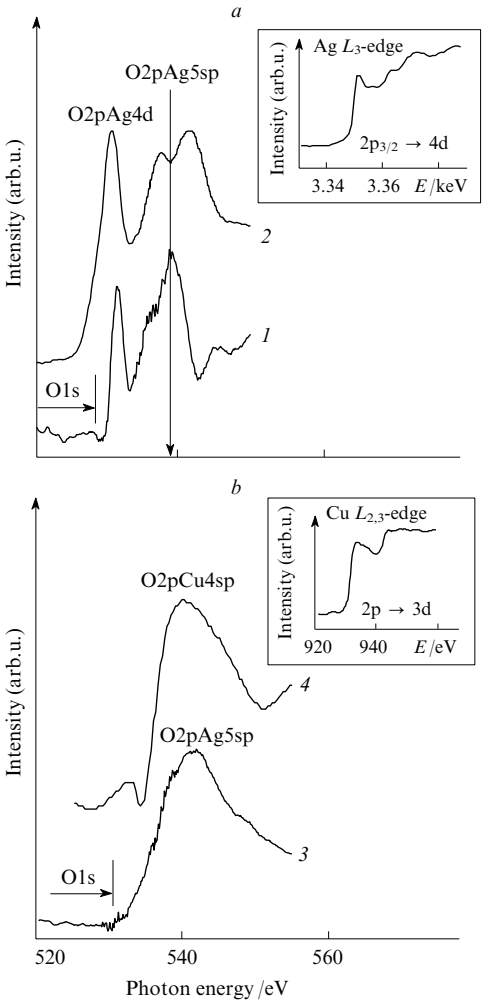


Figure 9. *K*-Edge XANES spectra of the nucleophilic form of adsorbed oxygen (O_{nucl}) (*a*, spectrum *1*) and oxygen within Ag_2O (*a*, spectrum *2*), electrophilic form of adsorbed oxygen (O_{elec}) (*b*, spectrum *3*) and oxygen adsorpbed on the copper surface (*b*, spectrum *4*).
Insets: *L*-edge spectrum of Ag_2O (*a*) and *L*-edge spectrum of the copper surface with adsorbed oxygen (*b*).[2, 3] The O1s binding energies from the XPS measurements for the respective samples are shown with horizontal arrows.

The oxygen XANES spectrum of bulk Ag_2O is very similar, which suggests similar electronic structures of $O(Ag_2O)$ and O_{nucl} (Fig. 9 *a*). The involvement of the silver 4d electrons into the formation of the Ag—O bonds in Ag_2O is also supported by the emergence of a 'white line' in the Ag L_3-edge XANES spectrum (3.352 keV, see inset to Fig. 9 *a*), which corresponds to the dipole-allowed electron transition $2p_{3/2} \rightarrow 4d$ ($\Delta l = 1$). An increase in the intensity of this line with an increase in the ionicity of the bond reflects the degree of the actual involvement of the silver 4d electrons in its formation.[96, 97] The transition $2p_{3/2} \rightarrow 4d$ is forbidden for an Ag^+ ion characterised by the electronic configuration $4d^{10}5s^0$. However, the formation of the chemical bond Ag—O results in electron density transfer from the 4d to the 5s orbitals. As a result, the electronic configuration of the Ag^+ ion can be formulated as $4d^{10-\delta}5s^{\delta}$, which features partly vacant 4d states near the Fermi level responsible for the emergence of a narrow X-ray absorption resonance at 3.352 keV.

The conclusions derived from the experimental XANES spectra are fully supported by quantum chemical calculations of the electronic structure of Ag_2O.[98] Indeed, the weak population of the Agd_{z^2} and Ag5s states indicates appreciable charge transfer from the Ag atom to the O atom associated with the Ag—O ionic bond formation. It is of note that this type of hybridisation (*viz.*, sd_{z^2}) is rather frequently observed for metals but rarely for ionic semiconductors like Ag_2O due to the wide energy gap between the occupied d-band and vacant sp-states. In terms of the molecular orbital theory, this can be reformulated in the following way. The O2p and Agd_{z^2} states are hybridised to form the pdσ bond, whereas the hybridisation of the O2p and Agd_{xz}, d_{yz} yields the pdπ bonds. These interacting orbitals are split into bonding and antibonding states with partial p- and d-characters. The $Agd_{x^2-y^2}$ and Agd_{xy} orbitals remain essentially non-bonding.[98]

The *K*-edge XANES spectrum of electrophilic oxygen species displays a broad peak around 541 eV (spectrum *3* in Fig. 9 *b*). The absence of distinct pre-edge peaks (around 531 eV) strongly implies that the Ag—O bonds are formed by the hybridisation of the oxygen 2p and silver 5sp electrons, whereas the metal 4d electrons remain unaffected. The respective $Ag3d_{5/2}$ spectrum does not show additional 'ionic' lines, such that the electronic state of the silver atoms is similar to that in the bulk metal [75] (the electronic configuration of silver atoms is $4d^{10}5s^1$). In the metallic state, the 5s electrons of silver are delocalised in the conduction band. Most likely, it is these delocalised conductivity electrons that participate in the formation of Ag—O_{elec} bonds.

According to the literature data, a similar oxygen XANES spectrum is characteristic of oxygen adsorbed on the copper surface in the suboxide state.[99] The respective Cu $L_{2,3}$-edge XANES spectra reveal no characteristic 'white line' in contrast to the spectra of CuO or Cu_2O (which are similar to that of Ag_2O), which means that the copper atoms in this structure indeed preserve essentially metal-like properties and only outermost 4sp electrons are involved in the Cu—O bond formation. Therefore, in both these cases, the M—O bonds are formed by the interaction of the oxygen 2p and metal outermost sp orbitals and characterised by the essentially covalent character.

Then another important question arises, what geometries can be ascribed to the adsorption complexes of O_{nucl} and O_{elec}. According to the literature data, the binding energy of O_{nucl} is $E_b(O1s) = 528.4 \pm 0.1$ eV (calibrated against the $Ag3d_{5/2}$ line with $E_b = 368.2$ eV) independent of the type of the silver surface [different polycrystalline foils, single-crystalline faces Ag(111), Ag(110) or Ag(100) and even graphite-supported silver particles]. The small scatter of the experimental data suggests the common character of the nucleophilic oxygen species adsorbed on different silver faces. The majority of researchers agree that the formation of the nucleophilic oxygen state is directly related to silver surface reconstruction. In particular, the oxygen adsorption on the Ag(110) crystal face at 300–500 K can give rise to the superstructures of the type Ag(110)-$(n \times 1)$-O, where n decreases from 7 to 2 with an increase in the O_2 exposure.[78, 100, 101] The Ag(110)-(2×1)-O reconstruction due to the appearance of supplementary atomic rows going along the [001] direction with the oxygen atoms residing nearly in the plane of the supplementary rows has been reliable established with scanning tunneling microscopy and photoelectron diffraction. The Ag–O bond length is 2.044 Å, which is nearly identical to the respective value typical of bulk Ag_2O (2.05 Å).[102] The formation of such a surface structure with $\Theta = 0.5$ monolayers results in a substantial (by 0.8 eV) increase of the work function as compared to clean silver surface, which indicates a significant charge transfer from the metal to oxygen atoms.[100] The linear increase in the work function with an increase in coverage implies that the surface dipole moment per adsorbed oxygen species is independent of coverage,[101] *i.e.*, the electronic structure of nucleophilic oxygen adsorbed on Ag(110) remains constant over the entire coverage range and is close to that in oxide. The adsorption of oxygen in the nucleophilic form on the densely packed Ag(111) face gives rise to the $p(4 \times 4)$ surface reconstruction. The nature of the Ag–O bonds in this surface structure is also believed (for instance, see Refs 10, 103 and 104) to be similar to that in bulk Ag_2O.

Thus, the nucleophilic form of oxygen is formed on the silver surface as a result of the reconstructive adsorption giving rise to linear fragments Ag–O–Ag (Fig. 10 *a*). Indeed, the angle Ag–O–Ag in both the bulk Ag_2O oxide and in the $Ag-O_{nucl}-Ag$ surface structure are close to 180°. Such a geometry favours the rather strong interaction between the silver 4d and oxygen 2p orbitals associated with the substantial charge transfer. The high ionicity of the Ag–O bonds in such a structure, on the one hand, provides the conversion of the silver atoms into the ionic form Ag^+ required for the ethylene adsorption and, on the other hand, determines the nucleophilic properties of the oxygen atoms in the ethylene epoxidation.

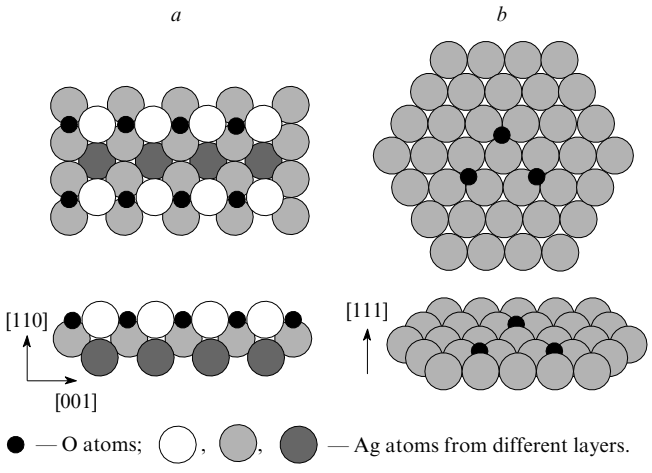


Figure 10. A structural model of adsorbed oxygen species.
(*a*) Nucleophilic oxygen on the reconstructed Ag(110) surface, (*b*) electrophilic oxygen on the unreconstructed Ag(111) surface. Top panels is top view, bottom panels is side view.

The geometry of the electrophilic oxygen state is less elucidated. It is only known from the experimental data that oxygen in the electrophilic form is adsorbed directly on the silver surface.[76, 79, 103] Most likely, the adsorption does not induce surface reconstruction and the oxygen atom is located above the triangle of silver atoms (three-fold hollow, Fig. 10 *b*). For instance, the adsorbed oxygen species with E_b(O1-s) = 530.1 eV have been detected on the Ag(111) face.[103] The absence of a surface reconstruction in that case was evidenced by LEED, whereas surface location of the oxygen atoms was confirmed by angular-resolved XPS. The absence of additional components in the Ag3d spectrum was consistent with the covalent character of the $Ag-O_{elec}$ bonds.

This model agrees well with the results of quantum chemical calculations. Zilberberg *et al.*[105, 106] found a stable state of atomically adsorbed oxygen on the non-reconstructed Ag(111) surface. The oxygen atoms are located symmetrically above a three-centre cavity and bound to three silver atoms [the three-fold axial symmetry is governed by the symmetry of the Ag(111) face]. The Ag–O bond length is 2.109 Å (note that the $Ag-O_{nucl}$ is 2.044 Å). The charge transfer from the metal to the adsorbate in this case should be much smaller than that in the binding of Ag to O_{nucl}. The aforementioned oxyradical oxygen adsorbed on Ag(110) is characterised by a similar geometry.[91, 92] In this case, oxygen is also localised on the three-centre position of the non-reconstructed surface, *i.e.*, the oxygen adsorption on Ag(110) proceeds dissociatively without reconstruction. Such a geometry of the adsorption complex determines the essential covalency of the Ag–O bond and consequently the electrophilic properties of this oxygen form in the ethylene epoxidation to ethelene oxide.

The experimental efforts aimed at the elucidation of the structure of the active site and the mechanism of the ethylene epoxidation have been described in so much detail to demonstrate that the *in situ* measurements provide correlation dependences sufficient to establish the structure–activity relationship in heterogeneous catalysis, despite they are associated with greater difficulties and ambiguities in data interpretations as compared to traditional UHV measurements. It is also evident that it is the application of several instrumental techniques to one system that gives a chance of success in establishing this relationship.

4. Reaction of partial methanol oxidation into formaldehyde over copper

As another example of efficient determination of the mechanism of a catalytic reaction using *in situ* measurements, we describe the methanol oxidation into formaldehyde over the copper surface studied by XANES, XPS and mass-spectrometry.[29, 35, 107] A brief survey of experimental facts available in the literature indicates that:

— a Cu catalyst has to be activated prior to use;

— the methanol conversion pathway depends on the ratio of methanol/oxygen partial pressures in the reaction mixture and on the sequence of the reactants supply;

— stoichiometric copper oxides (Cu_2O and CuO) demonstrate low selectivity in the formaldehyde synthesis;

— Cu catalysts are transformed into Cu_2O after evacuation of the reaction medium or its fast cooling aimed at the freezing of the active state of the copper surface.

This means that the forms of adsorbed oxygen responsible for the copper activity towards the selective methanol oxidation are formed directly under the reaction conditions. Thus, the catalytic system represents a dynamic system, which exists only

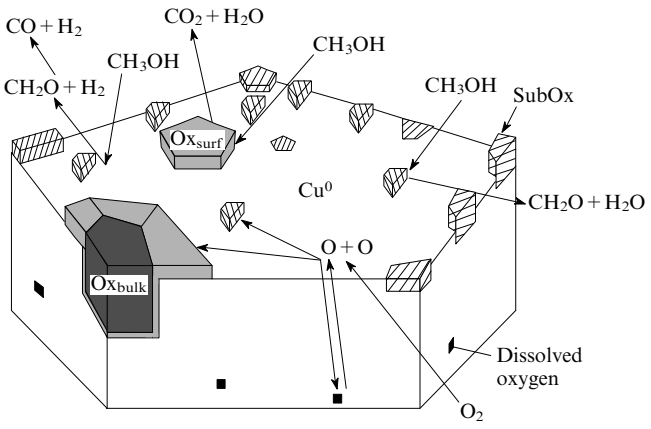


Figure 11. A model of the active surface of a copper catalyst with various co-existing oxygen species.[107]
The arrows indicate routes of mutual tranformations of various oxygen species and interaction paths of CH_3OH(gas) with the copper surface. Bulk (Ox_{bulk}) and surface (Ox_{surf}) oxide forms of oxygen catalyse the total methanol oxidation into CO_2 and H_2O. Formaldehyde is formed upon the interaction of methanol with weakly bound oxygen species (SubOx) adsorbed on the copper surface.

in the contact with the reaction medium and thus the 'pressure gap' problem is very important for this system.

As a result of studies, various forms of adsorbed oxygen have been identified and correlations between their concentrations and yields of respective products of the methanol oxidation via different pathways (*i.e.*, total or partial oxidation, *etc.*) have been determined. The surface oxygen species identified include two oxide forms (a surface and a bulk forms) and one suboxide form. The assignment of the latter to the a suboxide oxygen state was based on the absence of a characteristic O1s → O2pCu3d peak in the oxygen K-edge XANES spectra. Judging from the linear correlation between the surface concentration of suboxide oxygen and formaldehyde yield, it was concluded that it is this form that catalyses the partial methanol oxidation.[29, 107] Similar dependences of the formaldehyde yield on the concentration of the oxide forms were far from the linear character, which allowed a conclusion that these forms catalyse the total methanol oxidation.

A generalised scheme of various species present on the copper surface in the course of the catalytic methanol oxidation and responsible for different reaction pathways is shown in Fig. 11.[107] It is of note that the suboxide oxygen form on the copper surface was detected by means of XANES only in the presence of the reaction medium, which additionally demonstrates the importance of *in situ* studies.

A great interest of researchers to the state of active catalyst surfaces during their operation (even in the case of model systems) is reflected in the appearance over recent years of numerous monographs and special issues of scientific journals devoted to the application of instrumental techniques to studies of the catalytic activity in the *in situ* mode with surface-sensitive techniques occupying a notable place among them.[107–111]

III. The 'material gap' problem

The intermediate state occupied by nanoparticles in the row metal–atom determines their unique physicochemical properties (electronic, magnetic, optical, *etc.*) clearly distinguishable from those of both bulk metals and isolated atoms. No doubt, it is the changes in the surface structures and electronic properties of metal catalysts upon transition from bulk samples to nanoparticles that are of primary interest for catalysis specialists,[18–20] since it is these characteristics that govern the features of the interaction of reactants with the active component, the nature and reactivity of adsorbed species and ultimately the activity and selectivity of nanostructures in heterogeneous catalysis.

1. CO oxidation over nanoparticles of the platinum-group metals

According to investigations into the catalytic activity of palladium particles supported on α-Al_2O_3 with respect to the CO oxidation as a function of the mean particle size,[112] a decrease in the particle size from 30 nm to 5 nm accelerates the reaction three fold. This experimental fact was explained within the Langmuir–Hinshelwood mechanism, which assumes that any adsorption–desorption steps of a heterogeneous catalytic reaction are in equilibrium and the total rate is limited by the reaction between the adsorbed species:

$$CO_{gas} \rightleftharpoons CO_{ads},$$

$$O_{2,\,gas} \rightleftharpoons 2\,O_{ads},$$

$$CO_{ads} + O_{ads} \longrightarrow CO_{2,\,gas}.$$

In the case of CO oxidation of single-crystalline surfaces, the validity of this mechanism has been established earlier.[1, 113] An increase in the rate of the CO oxidation on Pd particles was explained by weaker binding of the CO molecules to the Pd atoms of small clusters. This conclusion was derived from a comparative TPD analysis of the CO adsorption on Pd(111) single crystal and disperse palladium samples.[1, 49] In the case of Pd nanoparticles with a size of 2.5 nm, the TPD spectrum of carbon monoxide reveals additional weakly bound states that are characterised by lower desorption temperatures as compared to adsorption states on the single-crystalline surface. Meanwhile, in the case of large particles with $d = 27$ nm, the TPD spectrum was identical to that measured with the single crystal.

A different in principle picture was observed for Pt particles supported on alumina[47] or mica:[114] the TPD spectra of CO desorption showed that a weakly bound state typical of a single-crystalline surface or large supported particles virtually disappears for Pt particles smaller than 3 nm. This observation is in accord with a more than seven fold deceleration of the CO oxidation on small Pt nanoparticles.[115] According to TPD studies of the CO adsorption on supported platinum and rhodium particles,[116] relative populations of weakly and strongly bound CO_{ads} is virtually independent of the mean size of rhodium dispersed particles. This explains why the reaction of $CO + O_2$ on the rhodium surface is structure-insensitive.[117]

The above example demonstrates that the use of model catalysts prepared by the thermal deposition of a metal on planar substrates is extremely efficient for the analysis of size effects for reactions catalysed by supported metal particles. This statement can be most spectacularly illustrated with a study of the CO oxidation on gold particles. Presently, this reaction became a canonical example of the 'nanosize' effect.

2. CO oxidation over gold nanoparticles

For a long time, gold was considered as one of the most inert metals. Nevertheless, as was discovered in the 1990s, gold nanoparticles with a size of < 5 nm supported on titania manifested high catalytic activity in a series of practically important reactions exceeding that of platinum catalysts traditionally applied in the field (the CO oxidation was the first reaction of this series[118, 119]). Figure 12 plots the atomic catalytic activity of nanosized gold particles for the CO oxidation reaction as a function of the mean particle size.[120, 121] It is clearly seen that the reaction rate rapidly increases with a decrease in the mean size of gold particles to

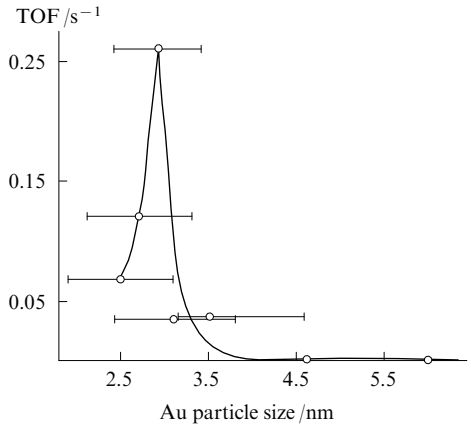


Figure 12. Turnover frequency (TOF) of the supported Au/TiO_2 catalysts with high specific surface areas in the CO oxidation at 300 K as a function of the mean Au particle size.[121]

3.5 nm. Further decrease in the particle size results in a decrease in the catalytic activity. Such an unusual catalytic behaviour of utrasmall Au particles remained unexplained at the atomic level for a long time despite enormous efforts put forth. The understanding of the size effect has been achieved owing to a transition to Au/TiO_2 model systems.[122–127] These brilliant results have been obtained by a group of researchers from the A&M University (Texas, USA) headed by Prof. Goodman.

A typical STM pattern for a model sample composed of gold nanoparticles with a diameter of 2.6 nm and a height of 0.7 nm (which constitutes only 2–3 atomic layers) dispersed on the $TiO_2(110)$-1×1 single-crystalline face and covering 25% of its surface is shown in Fig. 13. Such a morphology of the gold particles is explained by the fact that the growth proceeds in two steps: first two-dimensional (2D) islets are formed and only then as the surface concentration of gold increases, the particles start to grow in the third dimension.[128, 129] By changing the surface concentration of deposited gold, a series of model samples was prepared with the mean particle size systematically varying from 1.5 nm to 6 nm.

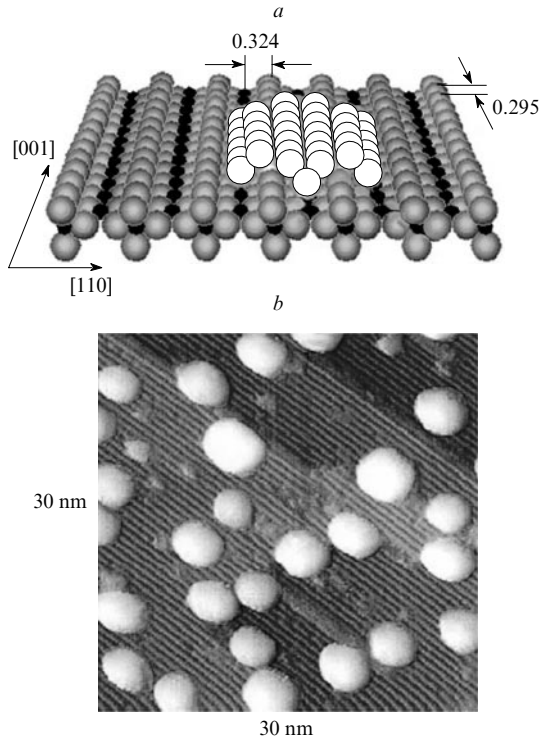


Figure 13. A structural model of bilayer Au islets on the $TiO_2(110)$ surface (*a*) and STM image of the $Au/TiO_2(110)$-(1×1) surface at $\Theta(Au) = 0.25$ monolayers (*b*).[127]

These model catalysts $Au/TiO_2(110)$-1×1 were assayed in the catalytic activity in the CO oxidation. The reaction rate as a function of the gold particle size obtained (Fig. 14) was nearly identical to that measured for real supported catalysts, which justifies the utilisation of model systems in the analysis of the size effects. The apparent activation energy in the temperature range of 350–450 K increases from 1.7 kcal mol^{-1} to 5 kcal mol^{-1} with an increase in the mean Au particle size from 2.5 nm to 6 nm.

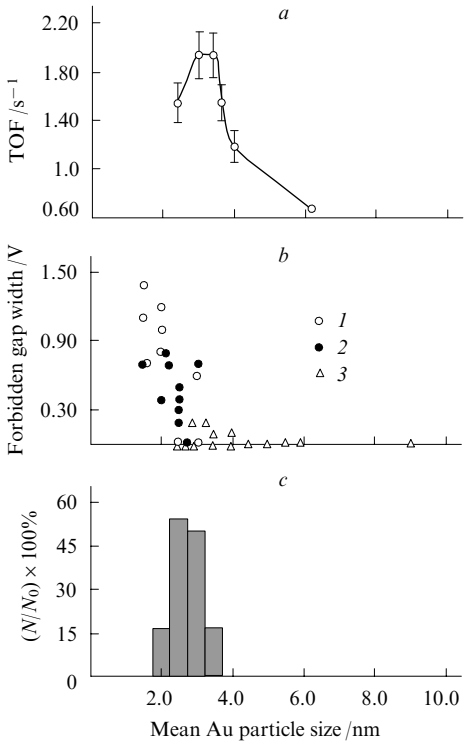


Figure 14. Turnover frequency (TOF) of the $Au/TiO_2(100)$ catalyst in the CO oxidation as a function of the mean Au particle size assuming their dispersion (*a*); changes in the band gap widths according to the STM measurements (*b*); relative coverage of the $TiO_2(100)$ surface with bilayer Au particles (*c*) as functions of the mean Au particle size. The data points *1–3* correspond to three samples with different gold concentrations.

These measurements on model samples helped to shed light upon the reasons for the extraordinary activity of gold nanoparticles. Variations in the mean size of particles in a range from 2 nm to 4 nm are accompanied by changes in the band gap (Fig. 14 *b*).[122, 127] With a decrease in the mean Au particle size below < 3.5 nm, a metal–insulator transition occurs:† particles with a height of one atomic layer are characterised by

† The metal–insulator transition, which is a particular case of the quantum size effect, was observed earlier for many metal catalysts.[124, 130, 131]

a rather wide band gap, whereas particles with heights of 3 layers and more are essentially metallic.

Furthermore, the strength of the CO – Au bond was shown to be dependent on the Au particle size. This conclusion was derived based on IR absorption spectroscopy of CO molecules adsorbed on gold nanoparticles with a size from 1.8 nm to 3.1 nm.[125,126] The specific heat of absorption abruptly increased from 12.5 kcal mol^{-1} to 18.3 kcal mol^{-1} with a decrease in the particle size, and the maximum is observed at the same size ($\sim$3 nm) as the catalytic activity maximum and the onset of the metal – insulator transition.[122] The final conclusion about the structure of active sites was made based on an analysis of the relative distribution of bilayer gold particles as a function of the mean particle size, which is also shown in Fig. 14 *c*. The maximum of this distribution falls on the same mean size (2.5 – 3.0 nm) as the maximum strength of the CO – Au bonds and activity of model catalyst in the CO oxidation.

Further arguments in favour of the suggestion that it is the bilayer gold particles that are active in the CO oxidation [33,101] were gathered in an LEED study of gold particles deposited into an ultrathin single-crystalline film of TiO_2. The film was prepared by mild oxidation of a titanium monolayer grown on a Mo(112) single crystal.[127] The surface was characterised by a distinct (8 × 2) LEED pattern. Two-dimensional gold islets and bilayer particles were identified by the appearance of (1 × 1) and (1 × 2) LEED patterns, respectively. The sample contaning bilayer gold particles manifested an unprecedented catalytic activity in the CO oxidation (Fig. 15). Thus, it was demonstrated that in order to provide high activity of nanosized gold catalysts in the low-temperature CO oxidation, gold particles composed of exactly two layers of Au atoms have to be selectively prepared. This finding initiated extended experiments aimed at the development of methods for the synthesis of nanoparticles supported on porous alumina and design of advanced catalysts on their base (see Section V).

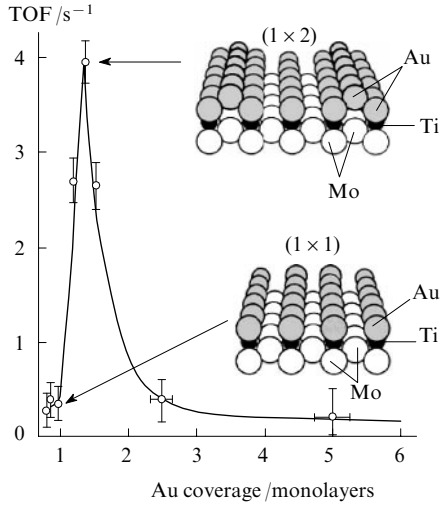


Figure 15. Turnover frequency (TOF) of the Au/Mo(112)-(8 × 2)-TiO_x catalysts in the CO oxidation at 300 K as a function of coverage of the surface with gold nanoparticles.

Model samples synthesised by the UHV deposition of metals on planar supports were used to study many aspects of the catalytic action of supported metal catalysts. Only a few of them will be addressed in the present review, including the catalytic synergism in the CO oxidation on bimetallic Pt – Rh catalysts,[132–135] the size effects ‡ in the ethylene epoxidation on silver catalysts [20,136–138] and the deactivation mechanism of Pt/Al_2O_3 catalysts for neutralisation of exhaust gases in the presence of SO_2.[139,140]

3. CO oxidation on bimetallic Pt – Rh catalysts

The synergism in the CO oxidation on supported $Pt-Rh/Al_2O_3$ catalysts used for the exhaust gases neutralisation has been reported for the first time by Oh and Carpenter,[141] who studied this reaction under conditions of excess of oxygen. They showed that catalysts prepared by successive impregnation of alumina with solutions of platinum and rhodium salts manifest significantly higher activities than mechanical mixtures of two catalysts with individual metals. This result was later reproduced by Cai *et al.*[142]

On the other hand, Nieuwenhuys *et al.*[143,144] observed no synergistic effect in the $Pt-Rh/Al_2O_3$ catalytic system. They noted only a monotonic change in the catalytic properties between two limiting points represented by monometallic platinum and rhodium systems. This apparent discrepancy was likely due to variations in the nature of studied samples, experimental conditions and procedures used for the catalysts preparation.[141–144] Nieuwenhuys *et al.*[143,144] employed simultaneous impregnation of alumina with a solution of platinum and rhodium salts, whereas Oh and Carpenter [141] and Cai *et al.*[142] performed the impregnation successively in two steps. It would be reasonable to assume that a statistical distribution of alloy particles over the alumina surface is realised in the case of the simultaneous impregnation and subsequent reduction, whereas isolated Pt and Rh particles are generated upon successive impregnation.

In order to verify this assumption, Bukhtiyarov *et al.*[132–135] carried out a comparative analysis of the CO oxidation on continuous polycrystalline films of Pt and Rh, their alloy and heterophase Pt – Rh bimetallic surfaces at a reaction mixture pressure below 10^{-5} mbar. The high-vacuum conditions were necessary to exclude surface oxidation of the catalysts, which cannot be avoided with porous supports.[141,142] Continuous polycrystalline films of Pt and Rh were prepared by UHV deposition of the respective metals on a Ta foil. In order to suppress the diffusion of the noble metals into tantalum, the surface of clean Ta foil was covered with a thin alumina film prior to metal deposition.[132]

The alloy with a composition of 56 at.% of Pt and 44 at.% of Rh was prepared by successive deposition of platinum and rhodium from two independent sources. Prior to experiments, the alloy was annealed at 800 °C for 10 min under UHV to equilibrate the atomic distribution.

The preparation of heterophase Pt – Rh surfaces included several steps: (a) vacuum deposition of a continuous rhodium film on the Al_2O_3/Ta substrate; (b) total oxidation of rhodium to Rh_2O_3 by exposure to oxygen for 30 min at $P = 10$ mbar and $T = 400$ °C; (c) vacuum deposition of Pt on the oxidised rhodium surface until the $Pt4f_{7/2}/Rh3d_{5/2}$ line intensity ratio in the XPS spectrum becomes equal to 0.38 and (d) subsequent reduction of the surface in hydrogen at $P = 10^{-6}$ mbar and $T = 300$ °C. The heterophase surface prepared in this way can be regarded as a model of catalysts synthesised by successive impregnation, whereas the alloy surface mimics the catalysts produced by simultaneous impregnation.

According to an STM study of these samples, the heterophase surface is composed of platinum particles with a size of

‡ As has been demonstrated earlier, the rate of ethylene oxide formation decreases by more than one order of magnitude with a decrease in the mean size of supported silver particles below 50 nm.

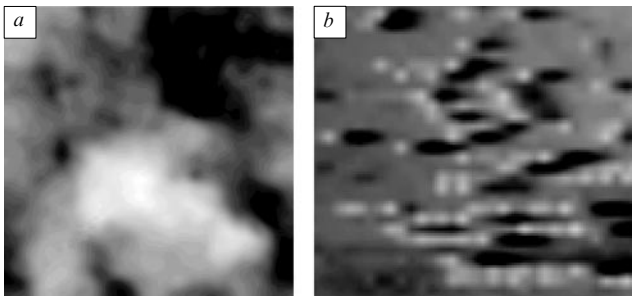


Figure 16. STM Images of the Pt–Rh alloy (*a*) and the Pt–Rh heterophase surface (*b*) prepared by the UHV Pt and Rh co-deposition on a thin alumina film grown on a Ta foil (see text).

10–20 nm dispersed on a flat rhodium substrate and covering 50% of its surface; the alloy is characterised by a smooth surface with a roughness of < 1 nm (Fig. 16). The heterophase surface is stable against heating up to 350 °C but converts into the homogeneous alloy at higher temperatures.

Typical plots of the CO oxidation rates (measured as a CO_2 partial pressure) for the platinum sample measured at a constant O_2 pressure (10^{-6} mbar) and variable CO pressures as a function of temperature are shown in Fig. 17. All curves reveal three distinct regions. At low temperatures, the reaction is very slow and the CO_2 concentration is below the detection limit of the mass spectrometer. With an increase in temperature up to a certain threshold value, CO_2 appears in the gas phase, then the reaction rate rapidly increases reaching the maximum value. After that, the reaction rate smoothly decreases. Similar dependences were obtained for all the samples under study.

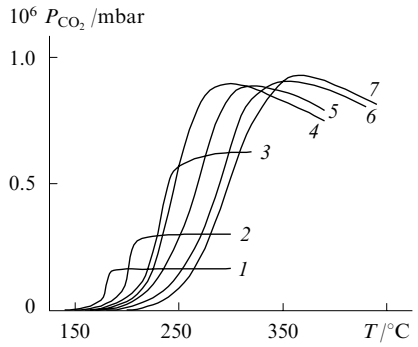


Figure 17. Temperature dependences of the CO oxidation rates (expressed as CO_2 partial pressures) on Pt as a function of P_{CO} at a constant oxygen pressure ($P_{O_2} = 10^{-6}$ mbar).
$10^7\ P_{CO}$ /mbar: 0.07 (*1*), 0.17 (*2*), 0.35 (*3*), 0.47 (*4*), 0.96 (*5*), 3.6 (*6*), 8.6 (*7*).

Such a character of the reaction rate *vs*. temperature plots is typical of platinum metals and explained by the adsorption mechanism of the CO oxidation (the Langmuir–Hinshelwood mechanism), which involves steps of reversible molecular adsorption of CO, dissociative adsorption of O_2 and a reaction between the adsorbed species on the metal surface.[1] At low temperature, the metal surface is covered by adsorbed CO molecules, which screen surface areas accessible to the O_2 adsorption. As a consequence, the reaction rate is low.

With an increase in temperature, CO_{ads} species partly desorb freeing adsorption sites for O_2. Under these conditions, the reaction rate is limited by the carbon monoxide desorption, *i.e.*, CO inhibits the reaction. With further increase in temperature, the reaction rate rapidly increases reaching the maximum value, which is accompanied by a change in the composition of the adsorbed layer from purely CO_{ads} to $CO_{ads} + O_{ads}$.[145] Further smooth decrease in the reaction rate with increasing temperature is usually attributed to the screening effects of adsorbed oxygen. At high temperatures, the reaction is characterised by the zero order with respect to the concentration of the excess of the reactant and nearly first order with respect to the concentration of the deficient reactant.[1]

Due to the validity of the Langmuir–Hinshelwood mechanism for the CO oxidation, the temperature dependences of the CO conversion known as the 'light-off curves' came in use as an industrial test of properties of catalysts for the afterburning of exhaust gases. Typically, the light-off curve has a shape similar to the above curves of the CO oxidation rates measured in a chamber of an XPS spectrometer serving as a catalytic reactor (see Fig. 17): the CO conversion is negligible at low temperature but rapidly increases reaching 100% when temperature is increased above the critical value. This fact can easily be rationalised taking into account that CO_2 is the only product of the CO oxidation. A catalyst that provides the minimum temperature of the 100% CO conversion is considered to be the best one (the half-conversion temperature is routinely used in quantitative comparisons).

In order to verify the probable synergistic effects for the heterophase surfaces, the temperature dependences of the CO oxidation rates were compared for different model surfaces, including monometallic Pt and Rh films, the Pt–Rh alloy and the Pt–Rh heterophase surface (Fig. 18). For the sake of comparison, Fig. 18 also shows a calculated temperature dependence of the CO oxidation rate on a bimetallic Pt–Rh sample with two independent platinum and rhodium domains with areas twice smaller than those in the individual monometallic samples (curve *5*). The number of platinum and rhodium surface sites in the case of the calculated curve was adjusted to be the same as in the heterophase surface. All experimental curves were measured under identical conditions for equimolar CO and O_2 mixtures ($P \approx 10^{-6}$ mbar).

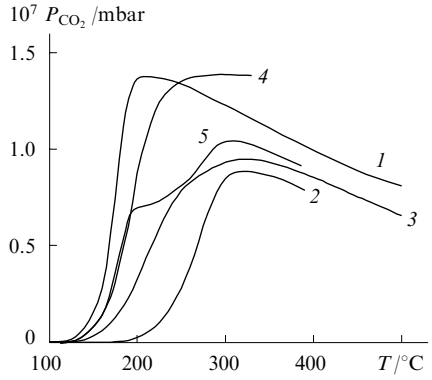


Figure 18. Temperature dependences of the CO_2 formation rates at $P_{CO} = P_{O_2} = 10^{-6}$ mbar on Rh (curve *1*), Pt (*2*), Pt–Rh alloy (*3*), Pt–Rh heterophase surface (*4*).
The simulated dependence for a heterophase Pt–Rh surface assuming independent Pt and Rh domains with relative coverages of 0.5 (curve *5*, see text).

As it becomes clear from Fig. 18, rhodium manifests much higher activity than platinum. Importantly, high oxidation rates are observed on the Rh catalyst at relatively low temperature. In particular, the activity of rhodium is maximum at $T = 200$ °C where platinum exhibits nearly zero activity. The activity of the alloy is intermediate between those of individual Rh and Pt. The CO oxidation rate on the heterophase surface is

close to that on rhodium at low temperatures and exceeds that on rhodium above 250 °C. Nevertheless, it has to be taken into account that the accessible area of rhodium in the case of the heterophase samples is twice smaller than in the case of the purely rhodium sample. Therefore, a comparison of the activity of the heterophase sample (curve *4* in Fig. 18) with the calculated curve (curve *5*) would be more informative. The calculated curve has a kink at $T = 200$ °C corresponding to the maximum reaction rate on pure rhodium and a maximum at $T = 300$ °C (corresponding to the maximum reaction rate on platinum).

The curves *4* and *5* are nearly identical at $T < 200$ °C, while the CO oxidation rate on the heterophase Pt – Rh surface starts to significantly exceed the respective value expected for the bimetallic surface under assumption of the independent behaviour of Pt and Rh domains at higher temperatures, *i.e.*, there is a prominent synergistic effect. This result was explained by a specific structure of the adsorption layer and its evolution in the course of the reaction (Fig. 19). At the ignition temperature, the adsorbed CO molecules are oxidised by O_{ads} species adsorbed on the rhodium regions that become vacant due to the CO desorption. The CO oxidation rate is maximum at $T = 200$ °C, which corresponds to the T_{max} for pure Rh. At this temperature, the reaction rate on platinum is low (since Pt particles are covered with CO_{ads}). At $T > 200$ °C, the reaction between CO_{ads} (on platinum) and O_{ads} (on rhodium) takes place (see Fig. 19). The experimentally observed synergism in this case is due to the involvement of the Pt particles into the overall process as a supplier of one of the reactants (*i.e.*, CO_{ads}).

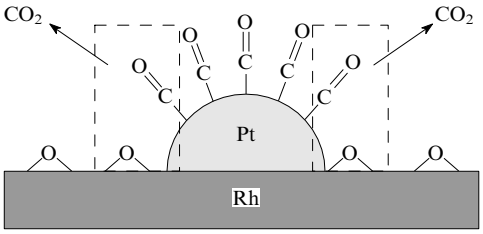


Figure 19. A structural model for the active Pt/Rh surface explaining the synergism in the CO oxidation.

In summary, the enhanced activity of the bimetallic catalyst can be explained by the selective adsorption of the reactants on different surface sites (O_{ads} preferably on rhodium whilst CO_{ads} preferably on platinum) and a reaction between the O_{ads} and CO_{ads} proceeding at the interface between Pt and Rh.

4. Interaction of oxygen with silver nanoparticles

The size effects in the ethylene epoxidation on silver catalysts were elucidated on model catalysts prepared by vacuum deposition of silver on the graphite substrate.[20, 136 – 138] The use of the carbon substrate instead of the oxide (Al_2O_3) helped to suppress the charging effects, which hampers studies of the electronic properties of supported metals by means of XPS for dielectric samples, and get rid of the masking O1s signal from the substrate. The absence of the spurious O1s from the substrate makes the XPS method highly informative for the elucidation of O_2 adsorption on the surface of supported silver particles.[137, 146] Sputtering of silver and subsequent oxygen adsorption on model Ag/C specimens was performed directly in a UHV chamber of a photoelectron spectrometer avoiding air exposure of the specimens. Only the STM characterisation of the supported silver particles was performed in a vacuum chamber of the tunneling microscope following transfer of the samples from the chamber of the photoelectron spectrometer.

A typical STM pattern of the graphite surface after the silver deposition (relative coverages were estimated according to ratios of the silver and carbon line intensities in the XPS spectra; the current sample corresponds to $I_{Ag3d}/I_{C1s} = 0.13$) is shown in Fig. 20. The originally rather smooth graphite surface becomes substantially rough after the silver deposition due to the formation of three-dimensional silver nanoparticles with a mean size of 1 – 3 nm. A statistical treatment of several (> 10) STM pictures afforded a size distribution histogram of silver particles depicted in Fig. 20 *b*. This sample is characterised by a mean silver particle size of 1 – 1.2 nm. Samples with larger mean particle sizes were prepared using longer deposition times, although this necessarily resulted in broadening of the size distribution.

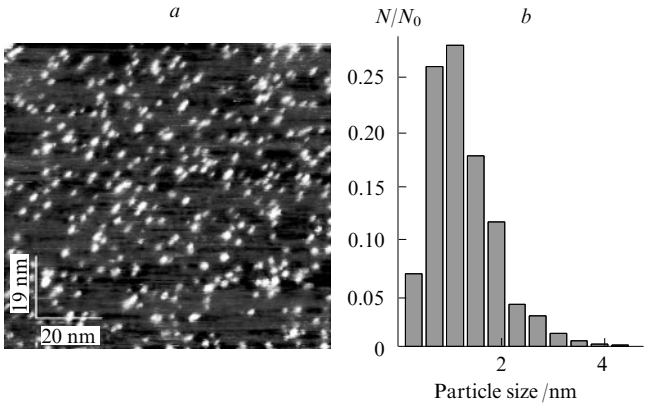


Figure 20. A typical STM image of the highly oriented pyrolytic graphite surface with deposited silver particles (*a*) and the respective size distribution histogram of the silver particles (*b*).

The O1s XPS spectra recorded just after the O_2 adsorption on Ag particles (within 10 min) at $P_{O_2} = 0.1$ mbar and $T = 420$ K are shown in Fig. 21. Only nucleophilic O_{ads} species are formed under these conditions on the bulk silver

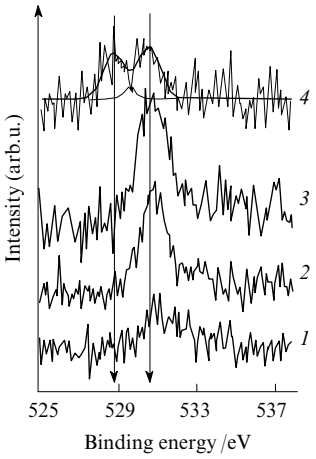


Figure 21. O1s XPS Spectra after exposure of graphite-supported silver particles to O_2 for 10 min at $T = 420$ K and $P_{O_2} = 0.1$ mbar as a function of coverage (estimated as the I_{Ag3d}/I_{C1s} line intensity ratio).
Coverage (particle size): (*1*) 0.13 (1 – 2 nm), (*2*) 1.5 (5 – 7 nm), (*3*) 2.4 (~ 10 nm), (*4*) 13.1 (> 20 nm). The mean size of Ag particles (in parentheses) was estimated from STM.

surface, whereas the electrophilic species are found on the nanoparticles, which is evidenced by the appearance of the O1s component with $E_b \approx 530.5$ eV in the XPS spectra. The electrophilic form of adsorbed oxygen remains prevailing for silver nanoparticles with sizes of up to 30 ± 10 nm. Only for larger Ag particles, the line characteristic of the nucleophilic oxygen species emerges in the spectra.

This result indicates that the same two species of adsorbed oxygen (*viz*., the nucleophilic and electrophilic ones) can be detected on the surface of supported silver nanoparticles as on bulk samples. They are formed directly upon adsorption of pure O_2 rather than of a mixture of oxygen and ethylene, which was necessary for the formation of the O_{elec} species in the case of bulk silver. This enables the collection of reliable TPD data for the electrophilic oxygen to estimate the strength of the $Ag-O_{elec}$ bonds. This was impossible for bulk silver due to a parasitic desorption contribution from oxygen dissolved in silver and O_{elec} elimination through the interaction with near-surface carbon (both dissolved oxygen and near-surface carbon are generated upon the activation of the bulk silver surface by the reaction medium).

The procedure used for the preparation of Ag/C samples was slightly modified for the determination of the strength of the Ag—O bonds by means of TPD. A thin film of graphite (with a thickness of a few hundred nm) was deposited on a Ta foil by pyrolysis of ethylene at $T = 1100$ K and $P = 50$ mbar.[137] The Ta foil was used as a resistive heater, which provided a sample heating rate of $2-3$ K s^{-1} sufficient for the TPD data acquisition. The time of ethylene pyrolysis was monitored by repeating survey XPS scans: the pyrolysis was stopped when the tantalum line was completely suppressed. The graphite-like nature of the carbon deposit was confirmed by XPS: the position of the C1s line and the appearance of a characteristic shake-up satellite were fully consistent with the respective features in the spectrum of bulk graphite.[146] The graphite layer was prepared in the same UHV chamber where subsequent vacuum deposition of silver and oxygen adsorption were carried out.

Figure 22 shows the curves of temperature-programmed desorption of electrophilic oxygen measured using mass spectrometry by the appearance of O_2 in the gas phase (heavy line) and as changes in the intensity of the O1s component with $E_b = 530.5$ eV (fine line) after its differentiation and inversion (the procedure used for the conversion of XPS data into TPD spectra is described in detail elsewhere [147]). The full agreement

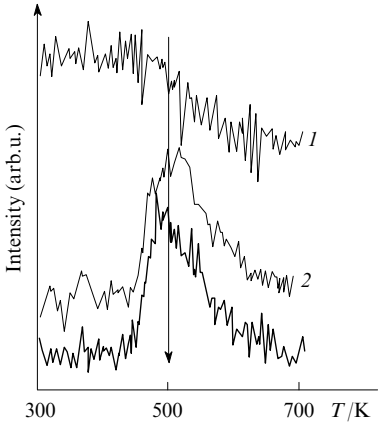


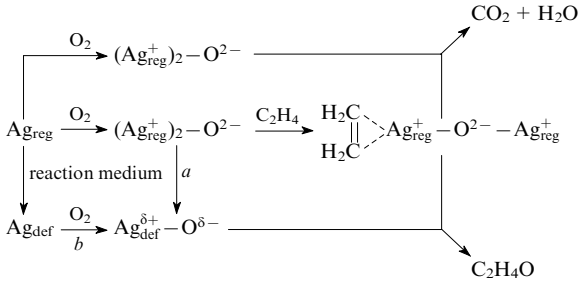
Figure 22. TPD Spectra of eletrophilic oxygen adsorbed on Ag particles measured by mass spectrometry (heavy line) and as changes in the XPS O1s line intensity for a relative coverage $I_{Ag3d}/I_{C1s} = 2.4$ [thin lines; (*1*) after differentiation, (*2*) after inversion].

of the TPD spectra obtained by mass spectrometry with that calculated from the XPS data confirms that the signal in both cases is due to the desorption of the electrophilic oxygen. According to these results, the electrophilic form of atomically adsorbed oxygen is characterised by a lower desorption temperature as compared to the nucleophilic form (500 K *vs*. 580 K), which means that this form responsible for the ethylene epoxidation is bound to the silver surface less strongly than the nucleophilic form, which is active in the total ethylene oxidation to CO_2 and H_2O. This conslusion is of great importance, since it confirms the compliance with the thermodynamical requirement of the possible participation of electrophilic oxygen in the formation of ethylene oxide: the upper limit of the bond strength for an oxygen species driving the epoxidation was estimated to $25-27$ kcal mol^{-1} (Refs 148 and 149).

The changes in relative amounts of the electrophilic and nucleophilic forms of O_{ads} on Ag/C catalysts dependent on the silver particle size is yet another feature of these catalysts. The character of this dependence (*i.e*., the disappearance of O_{nucl} with a decrease in the Ag particle size below $200-300$ Å) explains within a common mechanism the decrease in the rate of the ethylene epoxidation on $Ag/\alpha\text{-}Al_2O_3$ catalysts by more than an order of magnitude with a decrease in the mean size of silver particles down to 50 nm.[136] Indeed, the disappearance of the nucleophilic form of adsorbed oxygen on silver particles with a size < 50 nm results in a decrease in the concentration of adsorbed ethylene, which in turn results in deceleration of the key step of the epoxidation reaction, according to the active surface law. This result is another illustration that both the electrophilic and nucleophilic forms of oxygen adsorbed on silver are involved into the ethlyene epoxidation.[136–138]

Based on the results of fundamental investigations into the nature and reactivity of adsorbed oxygen species on supported silver particles, a mechanism of the ethylene epoxidation reaction was proposed (Scheme 1), which takes into account the silver surface morphology ensuring the formation of two forms of adsorbed oxygen.

Scheme 1



(*a*) Ag surface restructuring; (*b*) oxygen diffusion; Ag_{reg} and Ag_{def} are regular and defect domains of the supported silver particle surface.

The oxygen adsorption on a regular surface yields the nucleophilic adsorbed oxygen species, which promotes ethylene adsorption but is active only with respect to the total ethylene oxidation. Only transformation of regular surface domains into defect ones due to the silver activation under the action of the reactants enables the formation of the electrophilic form of O_{ads}, which upon interaction with adsorbed ethylene, affords the target partial oxidation product, ethylene oxide. Alternatively, the formation of the electrophilic form is also possible upon the direct adsorption of O_2 on defect sites of the silver surface. In particular, the surface of supported silver nanoparticles with a size of < 50 nm consists of electron density-deficient low-coordinated Ag atoms.[138]

The understanding of the molelcular mechanisms of catalytic reactions makes it possible to predict catalytic properties of specific catalysts and suggest possible ways of the improve-

ment of the existing catalytic systems. In particular, the yield of the target product, ethylene oxide, is one of the key characteristics of the epoxidation reaction on the industrial scale. In order to optimise the catalytic system as regards this parameter, the factors affecting the selectivity of the overall process have to be analysed. The selectivity of the reaction (S) with respect to ethylene oxide

$$S = \frac{R(C_2H_4O)}{R(C_2H_4O) + R(CO_2)}$$

is determined by the rate ratio of two competing reaction pathways, *viz*., epoxidation [$R(C_2H_4O)$] and total oxidation [$R(CO_2)$].

In the case of bulk silver samples, the nucleophilic oxygen species are formed efficiently, while the rate of the electrophilic form formation due to the modification of surface by components of the reaction medium is rather low. This favours the total oxidation pathway of the reaction. As a result, the selectivity of the epoxidation reaction rarely exceeds 30%–40% with silver single crystals, despite its relatively high rate.[8–10, 150]

When supported catalysts are used, the epoxidation reaction is decelerated by two orders of magnitude due to the low concentration of sites suitable for the ethylene chemisorption. But at the same time, the rate of the ethylene total oxidation by nucleophilic oxygen species also decreases and decreases more abruptly than that of the epoxidation. This is due to diffierent stoichiometries of the two oxidation pathways: the total oxidation of a C_2H_4 molecule to CO_2 and H_2O requires six oxygen atoms, whereas only one oxygen atom is needed for the partial oxidation. This results in a substantially enhanced selectivity of the partial oxidation of C_2H_4 in the case of supported catalysts[151] (S drops below 50% only in rare cases). If the mechanism of the ethylene oxidation reaction described above is valid, further decrease in the mean silver particle size (especially down to 50 nm and smaller) should further enhance the selectivity of the partial C_2H_4 oxidation (>86%, which is the maximum possible value realisable for molecular oxygen as the ethylene epoxidising agent; $S < 6/7$).[9, 10]

Notwithstanding, several authors (for instance, see Ref. 152) reported on a decrease in the selectivity on going to very small silver particles, which cannot be rationalised without postulated secondary reactions of ethylene oxide afteroxidation on the alumina surface. Ethylene oxide is formed exclusively on the silver surface (see above). Meanwhile, the total oxidation products, CO_2 and H_2O, can be generated in at least two pathways, *viz*., the interaction of C_2H_4 with the nucleophilic oxygen species adsorbed in silver and the afteroxidation of ethylene oxide. It is well known that it is the reaction proceeding on the alumina surface that makes the dominant contribution to the afteroxidation pathway. Its rate is independent of the mean size of supported silver particles. This implies that the side reaction of the ethylene oxide afteroxidation has to be suppressed in order to increase the selectivity of the partial ethylene oxidation. Taking into account that this reaction is catalysed by acidic OH-sites present on the alumina surface,[153] the use of surfaces devoid of such sites can serve as a possible solution of the problem. Indeed, Balzhinimaev *et al.*[154] achieved the selectivity of the ethylene epoxidation as high as 85%–88% by using a carbon substrate (sibunite) instead of alumina. Even higher selectivity (>90%) was achieved by the utilisation of utradispersed silver particles with a mean size close to the optimum (50–100 nm).[154] This results are the best confirmation of the validity of the proposed reaction mechanism and consequently of the efficiency of the fundamental approach to the design of catalysts based on experimental studies of model systems with surface science techniques discussed in the present review.

IV. Investigations into the structure of active sites in porous catalysts

The elucidation of the formation and evolution of active sites during the preparation, activation and deactivation of porous catalysts with surface science techniques constitutes an important part of the proposed investigation scheme (see Introduction), since it enables the transition from model objects to real catalytic systems. However this task is very demanding from the experimental viewpoint. First of all, difficulties in the interpretaion of the experimental results have to be taken into account, which are due to the complex stoichiometry and phase composition of real catalysts, low concentrations of the active component and high concentrations of promotors therein. In our opinion, a rational compromise between catalytic characteristics of a model catalyst and the relative simplicity of its structure is needed to make an advance in these investigations. Although preparation of such catalyst results in a decrease in its activity (however, this should not be dramatic), this is compensated for by more straightforward interpretation of the experimental results. In order to improve the reliability of structural information provided, one should supplement surface science techniques with traditional techniques of catalyst characterisation, such as TEM, X-ray diffraction, *etc*.

The history of ITSS application to the characterisation of porous catalysts is nearly as long as their utilisation for studies of chemical interactions on the surface of model samples; pioneering works in both directions date back to the 1970s. The number of studies in this field is so large that any their systematic analysis is near to impossible. Often the experimental results are reported as a mere characteristics of specific catalyst samples without recourse to respective results on appropriate model objects. Nevertheless, even these results are in some cases valuable for establishing the structure–activity relationships in heterogeneous catalysts within the fundamental approach discussed in the present review. First of all, this concerns systems where model catalysts do not possess sufficient catalytic activity under conditions accessible to instrumental characterisation (even in the *in situ* mode), *i.e*., where a catalytic reaction proceeds at a measurable rate only on a catalyst with high specific surface area. Ruthenium catalysts of the ammonia synthesis are typical expamples of such systems. Indeed, all attempts at the elucidation of the structure of possible ruthenium active sites with traditional model experiments failed due to the negligible activity of Ru single crystals with respect to N_2 adsorption (the respective N_2 sticking probabilities reported in the literature lie in the range of 10^{-12}–10^{-9}).[155–157] Meanwhile, catalytic, structural and spectral studies performed on porous Ru/MO_x, $Ru-Cs^+/MO_x$ (MO_x = MgO, Al_2O_3 or SiO_2) catalytic systems revealed important details of the promotor–metal and promotor–support interactions and helped to determine the active site structure.[158–160]

1. The promotion mechanism of ruthenium catalysts in the ammonia synthesis

Ruthenium-containing supported systems are widely recognised as the most promising and practical catalysts of the gas-phase ammonia synthesis at moderate pressures and temperatures. It is known that the activity of such catalysts in the ammonia synthesis is dependent on the chemical nature of the support: higher activity is provided by supports with prominent basic properties. The highest activity was achieved with magnesia.[161] The use of technologically more suitable supports, such as alumina or carbonaceous materials, instead of MgO results in a dramatic decrease in the activity of ruthenium

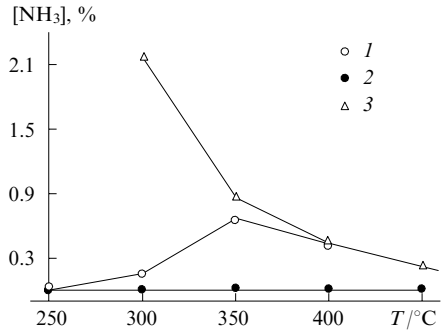


Figure 23. Steady ammonia concentration in the reaction mixture at the reactor outlet for the $Ru-Cs^+/MgO$ (curve *1*) and $Ru-Cs^+/Al_2O_3$ (curve *2*) catalysts as a function of temperature.
Equilibrium of the ammonia curve yield (*3*) calculated for the reaction conditions used in the experiment.

catalysts.[162, 163] The activity of supported rithenium catalysts can be enhanced to a level sufficient for industrial applications by doping with alkali metals or their compounds. The activity of ruthenium catalysts increases with an increase in the basicity of the dopant along the series $Na^+ < K^+ < Rb^+ < Cs^+$.[164]

The reasons and mechanisms underlying the influence of the support material and dopant type on the activity of supported ruthenium catalysts in the ammonia synthesis remains a subject of vivid scientific discussions, but no consensus has been reached so far. In order to make progress in this field, three types of interactions have to be considered: (1) between the catalytically active metal and promotor, (2) between the metal and support and (3) between the promotor and support.[158–160] Within the context of this study, magnesia, alumina and silica were tested as support materials, $Ru(OH)Cl_3$ and Cs_2CO_3 were chosen as precursors of the active component and promotor, respectively.

Studies of catalytic properties of promoted and non-promoted supported ruthenium systems differing in supports and precursors revealed $Ru-Cs^+/MgO$ samples to be the most active. Al_2O_3-Supported ruthenium is significantly less active than MgO-supported. Temperature dependences of the catalytic activities of two catalysts, *viz*., $Ru-Cs^+/MgO$ and $Ru-Cs^+/Al_2O_3$, expressed as steady-state ammonia concentrations in the reaction mixtures are presented in Fig. 23 together with the equilibrium curve of ammonia yield calculated for the reaction conditions. In the presence of the $Ru-Cs^+/MgO$ catalyst, the yield of ammonia nearly reaches its equilibrium value at $T = 350$ °C, whereas the $Ru-Cs^+/Al_2O_3$ catalyst is inert under these conditions. The performances of these two catalysts in the ammonia synthesis expressed as the amount of ammonia (ml) per g of the catalyst in 1 hour are listed in Table 1. The tabulated data also clearly confirm that $Ru-Cs^+/MgO$ is characterised by a significantly higher activity than $Ru-Cs^+/Al_2O_3$. A combination of instrumental techniques was used to analyse the reasons for the so different catalytic properties of the samples.

Table 1. Performance of the ruthenium catalysts in the ammonia synthesis measured at ambient pressure and a ratio of $H_2 : N_2$ partial pressures of 3 : 1.

Temperature /°C	$Ru-Cs^+/Al_2O_3$ /ml(NH_3) g(cat)$^{-1}$ h^{-1}	$Ru-Cs^+/MgO$ /ml(NH_3) g(cat)$^{-1}$ h^{-1}
250	0 [a]	0.4
300	0	4.4
350	0	19.8
400	0	12.7

[a] The lowest detection limit was less than 0.1 ml(NH_3) g(cat)$^{-1}\cdot$h^{-1} (the volume of NH_3 under normal conditions).

The results of XPS and AES studies on the electronic states of different ruthenium catalysts are given in Table 2. The binding energy of the ruthenium core level $E_b(Ru3d_{5/2})$ changes from 280.2 eV typical of bulk ruthenium to 279.0 eV or 280.4 eV in the $Ru-Cs^+/MgO$ and Ru/Al_2O_3 catalysts, respectively. The shift of Ru3d binding energies in MgO-supported catalysts (279.2–279.5 eV) with respect to bulk ruthenium suggests that the high activity of these samples is due to the charge transfer from the basic support (MgO) to the ruthenium nanoparticles.[163] The access of electron density on the ruthenium atoms facilitates the activation of a nitrogen molecule owing to the electron transfer from the 3d orbitals of Ru to the antibonding orbitals of N_2 (which is the first step of the dissociative N_2 adsorption). It is generally accepted that it is the nitrogen activation that is the rate-limiting step in the ammonia synthesis. In contrast to the Ru/MgO catalysts, the Ru/Al_2O_3 and Ru/SiO_2 samples are characterised by standard (normal) values of the binding energy close to that in bulk ruthenium (280.2–280.5 eV).[160, 163, 165]

Although the negative shift in the position of the core-level line in XPS spectra can indeed indicate an excessive electron density on the supported metal due to its interaction with the support, there are several other reasons (including non-chemical ones), which could be responsible for the effect observed. These include a change in the relaxation energy (which is the

Table 2. Relevant XPS parameters of the ruthenium catalysts.

Sample	$E_b(Ru3d_{5/2})_{exp}$ /eV	$E_{kin}(RuMNN)$ /eV	α /eV	ΔE_{relax} /eV	ΔE_{dif} /eV	$E_b(Ru3d_{5/2})_{corr}$ /eV
Ru_{bulk}	280.2	274.5	554.7	0	0	280.2
Ru/MgO	279.5	275.3	554.8	0	+1.0	280.5
Ru/Al_2O_3	280.4	274.3	554.7	0	+0.1	280.5
$Ru-s^+/MgO$	279.0	274.6	553.6	−0.6	+1.3	279.7
$Ru-Cs^+/Al_2O_3$	280.2	274.5	554.7	0	+0.4	280.6

Notations adopted: $E_b(Ru3d_{5/2})_{exp}$ is the $Ru3d_{5/2}$ core-level binding energy observed experimentally; $E_{kin}(RuMNN)$ is the kinetic energy corresponding to the *RuMNN* Auger peak (with the AlK_α excitation at 1488.6 eV); α is the modified Auger parameter calculated as $\alpha = E_b(Ru3d_{5/2}) + E_{kin}(RuMNN)$; ΔE_{relax} is a change in the relaxation energy calculated as $\Delta E_{relax} = 0.5\Delta\alpha$, where $\Delta\alpha$ is a difference in α between a supported catalyst and bulk Ru; ΔE_{dif} is a differential charging value determined from a comparison of the valence-band spectra as a difference between the Fermi edge positions for a supported catalyst and bulk Ru; $E_b(Ru3d_{5/2})_{corr}$ is the $Ru3d_{5/2}$ core-level binding energy corrected for the final state effects, *i.e*., $E_b(Ru3d_{5/2})_{corr} = E_b(Ru3d_{5/2})_{exp} + \Delta E_{relax} + \Delta E_{dif}$.

energy of the electron redistribution in the presence of a core hole generated upon photoemission, it is also referred to as the final-state effect) and a differential charging,§ *i.e.*, a smaller positive electrostatic potential of the surface of metal particles with respect to that of the dielectric support, which gives rise to different shifts of the respective core-level lines (a sample surface during XPS measurements is always charged positively to a certain steady value dependent on the dielectric properties of the material due to the constant emission of photoelectrons).

Neither relaxation nor differential charging effects can be estimated using the internal standard method (the positions of XPS lines in the spectra of supported catalysts are usually referenced to a selected line of an element from the support material). The change in the relaxation energy (ΔE_{relax}) can be determined from the change in the modified Auger parameter α for the supported metal with respect to the bulk metal. The modified Auger parameter α is calculated as the sum of the binding energy of a metal core-level and the kinetic energy of the respective Auger peak:[166]

$$\Delta E_{relax} = \frac{1}{2}\Delta\alpha = \frac{1}{2}\Delta\left[E_b(Ru3d_{5/2}) + E_{kin}(RuMNN)\right].$$

The extent of the differential charging (ΔE_{dif}) can be determined from the Fermi edge shift in the valence-band spectrum of supported metal particles with respect to its position in the spectrum of the bulk metal.[167, 168]

The values of parameters α, ΔE_{relax} and ΔE_{dif} determined for the Ru/MO_x and $Ru-Cs^+/MO_x$ supported systems from the XPS spectra are compiled in Table 2. The values of α for Ru/MO_x and Ru_{bulk} are identical to within 0.1 eV (554.7 – 554.8 eV), which implies that $\Delta E_{relax} \approx 0$ for non-promoted systems. Non-zero differential charging of Ru particles was observed only in the case of Ru/MgO ($\Delta E_{dif} = +1.0$ eV), whereas it equals to zero for Ru/Al_2O_3 and Ru/SiO_2. Thus the original experimental values of $E_b(Ru3d_{5/2})$ for Ru/Al_2O_3 and Ru/SiO_2 are correct, whereas the respective value for Ru/MgO has to be corrected to the differential charging:

$$E_b(Ru3d_{5/2})_{corr} = E_b(Ru3d_{5/2})_{exp} + \Delta E_{dif} =$$
$$= 279.5 + 1.0 = 280.5 \text{ eV}.$$

Therefore, taking into account the necessary corrections, the binding energy of the Ru atoms in the Ru/MgO system is essentially the same as in other Ru/MO_x systems studied exceeding the respective value of bulk ruthenium by $\Delta E = 0.3 \pm 0.1$ eV. The latter value means that the surface ruthenium atoms in the Ru/MO_x systems are slightly oxidised, which disproves the earlier assumption of the excess electron density on the MgO-supported Ru particles.

In the case of promoted samples (see Table 2), the experimental ruthenium binding energies $E_b(Ru3d_{5/2})$ are 279.0 eV and 280.2 eV for $Ru-Cs^+/MgO$ and $Ru-Cs^+/Al_2O_3$, respectively. The modified Auger parameter α for $Ru-Cs^+/MgO$ differs from that of bulk ruthenium by -1.2 eV, *i.e.*, in this case, $\Delta E_{relax} = -0.6$ eV. Furthermore, a non-zero differential charging was identified for both promoted systems $Ru-Cs^+/MgO$ ($\Delta E_{dif} = +1.3$ eV) and $Ru-Cs^+/Al_2O_3$ ($\Delta E_{dif} = +0.4$ eV). The true binding energies after all corrections, $E_b(Ru3d_{5/2})_{corr}$, are 279.7 eV and 280.6 eV for $Ru-Cs^+/MgO$ and $Ru-Cs^+/Al_2O_3$, respectively. Thus, a negative shift in the ruthenium binding energy with respect to bulk metal is observed for the promoted MgO-supported catalyst.

§ This possible reason for negative shifts of XPS lines is most frequently ignored, which is not actually justified.

The reasons for the negative shifts of the $Ru3d_{5/2}$ binding energy in this sample were found in additional studies, primarily, using TEM. Histrograms of the size distributions of Ru particles revealed that, in both supported Ru/MO_x systems and promoted samples, ruthenium particles are characterised by sizes in the range of 2 – 10 nm [160] or several nanometres, respectively, which rules out the possible assignment of the Ru3d line shift to a change in the mean Ru particle size. More details on the structure of the active component have been obtained using high-resolution TEM. The respective micrographs of promoted catalysts are shown in Fig. 24. In the case of $Ru-Cs^+/MgO$ (Fig. 24 *a*), it is clearly seen that the Ru particles are coated with a thin layer of a substance, while the Ru particles in the $Ru-Cs^+/Al_2O_3$ sample are devoid of such a coating (Fig. 24 *b*).

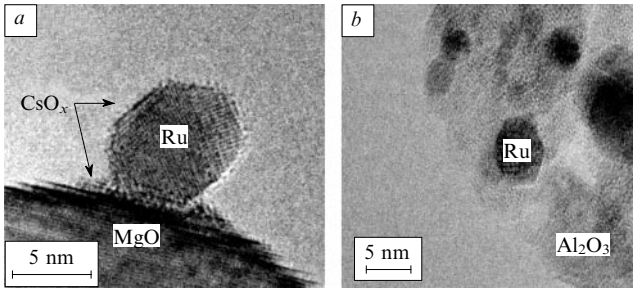


Figure 24. Electron micrographs of the surface of the $Ru-Cs^+/MgO$ (*a*) and $Ru-Cs^+/Al_2O_3$ (*b*) catalysts.

The nature of the surface coating of the Ru particles was identified by the Energy-Dispersive X-ray fluorescence analysis (EDX) implemented in an attachment to a transmission electron microscope (it provides a spatial resolution of < 100 nm).[160] The EDX spectra measured in the proximity of ruthenium particles for the $Ru-Cs^+/MgO$ and $Ru-Cs^+/Al_2O_3$ catalysts are compared in Fig. 25. In the case of $Ru-Cs^+/MgO$, the EDX spectrum reveals a weak peak attributed to Cs in addition to the dominant ruthenium signal, whereas no additional signal was detected for $Ru-Cs^+/Al_2O_3$. This result was consistently reproduced for a larger number of ruthenium particles.[160]

Data on CO chemisorption provide another experimental evidence for the formation of a Cs-compound on the surface of Ru particles in the catalyst $Ru-Cs^+/MgO$. It was

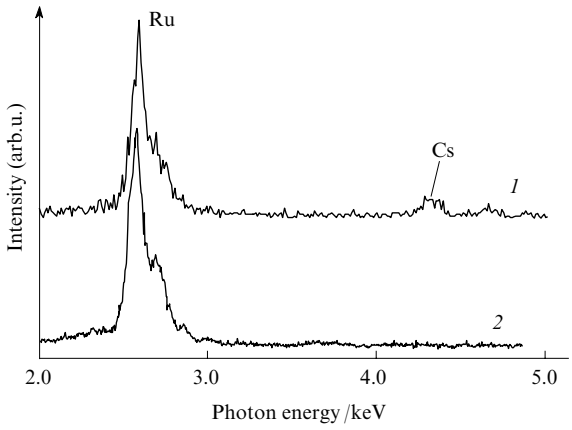


Figure 25. EDX Spectra from areas in the proximity of ruthenium particles for the $Ru-Cs^+/MgO$ (spectrum *1*) and $Ru-Cs^+/Al_2O_3$ (spectrum *2*) catalysts (see Fig. 24).

found that the degrees of dispersion D defined as $D = (N_{surf}/N_{tot}) \times 100\%$, where N_{surf} is the number of surface Ru atoms and N_{tot} is the total number of Ru atoms, in the promoted and non-promoted Al_2O_3-supported samples are nearly identical (D = 25.0% and 23.6%, respectively). Meanwhile, a totally different picture is observed for the analogous MgO-supported catalysts: the degree of dispersion D in the promoted sample decreases to 9.9% from 27.3% in the non-promoted sample despite no significant changes in the mean size of ruthenium particles is detected by TEM. This observation suggests that the surface of Ru particles accessible for CO adsorption in the latter sample is partly screened by the promotor. Presumably, this interaction between ruthenium and the promotor plays a key role in the formation of the active catalytic state, which is manifested in the negative shift of the $Ru3d_{5/2}$ line.[158–160]

The speciation of the promotor chemical state was accomplished based on the $Cs3d_{5/2}$ XPS data. Figure 26 shows the respective core-level spectra for $Ru-Cs^+/MgO$ (*a*) and $Ru-Cs^+/Al_2O_3$ (*b*) measured both immediately after loading of the samples into the spectrometer and after their reduction with hydrogen directly in the spectrometer. The efficiency of XPS for the identification of the caesium chemical state is demonstrated by Table 3, which compiles the $E_b(Cs3d_{5/2})$ values for various caesium compounds with oxygen.[169–171] The data given in Table 3 indicate that inverse chemicals shifts in the binding energy are typical of caesium, as well as for some other metals (Ag, Cd, Ba, *etc.*), *i.e.*, the binding energy decreases rather than increases upon oxidation. The reasons for this phenomenon lie beyond the scope of this review and will not be discussed here. It is important that the data from Table 3 help to assign the experimentally observed Cs3d spectral features to specific states of the caesium atoms or caesium compounds.

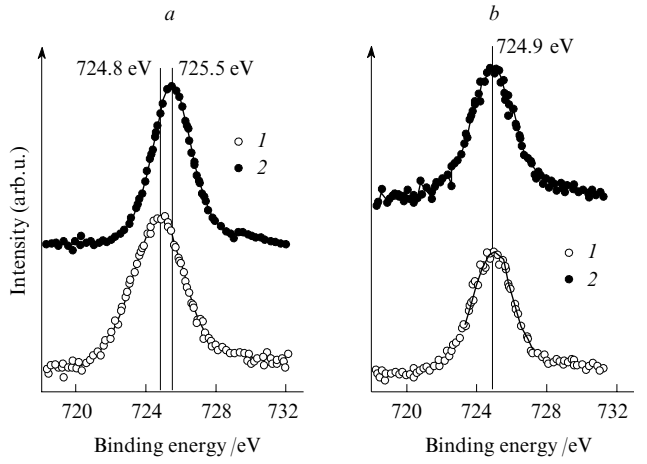


Figure 26. The $Cs3d_{5/2}$ XPS spectra of the $Ru-Cs^+/MgO$ (*a*) and $Ru-Cs^+/Al_2O_3$ (*b*) before (*1*) and after (*2*) hydrogen treatment directly in the spectrometer.

The XPS spectra of the $Ru-Cs^+/MgO$ and $Ru-Cs^+/Al_2O_3$ catalysts measured immediately after their loading into the spectrometer reveal nearly identical positions of the $Cs3d_{5/2}$ lines with binding energies of 724.8 eV and 724.9 eV, respectively (see Fig. 26). This caesium state can be attributed to Cs^+ (suggestedly, as caesium peroxide). Caesium in caesium oxide Cs_2O is characterised by a similar binding energy $E_b(Cs3d_{5/2})$ = 725.0 eV, but it is known that caesium oxide readily converts into peroxide upon exposure to oxygen

Table 3. $E_b(Cs3d_{5/2})$ and $E_b(O1s)$ values for various caesium compounds.[166–170]

Binding energy /eV	Cs compound					
	Cs_{met}	$Cs_{2+x}O$	Cs_2O	Cs_2O_2	Cs_2O_4	CsOH
$E_b(Cs3d_{5/2})$	726.1	725.5	725.0	724.5	724.2	724.1
$E_b(O1s)$	–	531	528.2	530.6	532.9	–

(exposure doses of $(5-10) \times 10^{-6}$ Torr s),[170] which quite decisively rules out its presence in the catalysts under study.

The reduction of the $Ru-Cs^+/MgO$ sample with hydrogen directly in the spectrometer leads to a shift of the $Cs3d_{5/2}$ line to larger binding energy, which is indicative of caesium reduction, whereas the spectrum of $Ru-Cs^+/Al_2O_3$ remains unchanged upon similar treatment. Meanwhile, the $Cs3d_{5/2}$ binding energy in promoted ruthenium-free samples on different supports shows no shifts due to oxidative or reductive treatments. The shift of Cs3d lines upon reduction of $Ru-Cs^+/MgO$ also supports the existence of direct caesium–ruthenium interactions.[160] Presumably, during the reduction, hydrogen molecules dissociate on the surface of ruthenium particles, which enables the subsequent reduction of caesium ions with atomic hydrogen.

The details of the interaction of caesium with ruthenium were established by XPS studies of model samples prepared by the deposition of caesium onto a polycrystalline ruthenium foil either in vacuum or in an oxygen flow. The $Cs3d_{5/2}$ and O1s binding energies and the Cs : O atomic ratios were determined. An analysis of these spectral data and, especially of the $E_b(O1s)$ values, which are highly specific for different caesium compounds with oxygen [170, 171] revealed that the vacuum deposition yields caesium suboxide $Cs_{2+x}O$, whereas that in an oxygen flow affords caesium peroxide Cs_2O_2. Some deviations of the experimental Cs : O atomic ratios from the stoichiometric values were attributed [160] to a partial oxidation of the suboxide due to an insufficiently high vacuum or concomitant formation of caesium superoxide Cs_2O_4 (in the cases of the $Cs_{2+x}O/Ru$ and Cs_2O_2/Ru layers, respectively). The presence of superoxide in the sample is evidenced by the emergence of an additional component with E_b = 533.5 eV in the O1s XPS spectrum.[172, 173]

Taking these results of model studies into account, it might be concluded that the $Cs3d_{5/2}$ binding energy in the range of 725.4–725.8 eV can be attributed to caesium suboxide (although its partial contamination with oxide cannot be ruled out), whereas the values in the range of 724.7–725.2 eV are due to caesium peroxide.

However, it has to be noted that, for the suboxide, this assignment means only the formation of surface species rather than an individual phase. Otherwise it would have been possible to observe these compounds by X-ray diffraction. At the same time, only metallic ruthenium and the respective support (MgO or Al_2O_3) were identified in the diffraction patterns of both non-promoted and promoted samples.[158–160] In earlier works devoted to Cs-promoted silver catalysts of the ethylene epoxidation, Podgornov *et al.*[173] suggested that silver atoms are capable of substituting for the Cs atoms in the Cs–Cs fragment present in the bulk structure of caesium suboxide to form the Cs–Ag bond.

Following this analogy, it might be suggested that bonds between the caesium and ruthenium atoms are formed in the catalyst $Ru-Cs^+/MgO$. This suggestion is further supported by the fact that the $E_b(Cs3d_{5/2})$ binding energy in promoted ruthenium blacks (*i.e.*, in support-free materials) increases from 725.0 eV to 725.5 eV upon their reduction in the spectrometer. Similar results were observed for thin films of caesium on the surface of bulk ruthenium. At the same time,

in the alumina-based systems, the $Cs3d_{5/2}$ binding energy remains constant irrespective of the oxidative or reductive treatment applied.

The experimental evidence presented above indicate that it is the ruthenium – promotor rather than ruthenium – support interactions that are responsible for the observed shift of the $Ru3d_{5/2}$ line to a smaller E_b.[158, 160] The formation of a thin alkali metal film on the surface of a transition metal is known to decrease the work function (*e.g.*, S1 caesium – silver photocathodes are formed in a similar way).[171] Thus, the downshift of the binding energy can also be due to a decrease in the work function of the electron escape from the surface of Ru particles covered with a promotor layer.

If this suggestion is valid, a next question arises, why ruthenium effectively interacts with caesium only with magnesia as a support, whereas no such interaction occurs on alumina. An answer to this question was given by an X-ray diffraction study of the $Ru-Cs^+/Al_2O_3$ and Ru/Al_2O_3 samples. The diffraction pattern of the promoted catalyst reveals some increase in the scattering backgound in the angle range of $20-40^\circ$,[160] which is typical of caesium aluminate. Most likely, caesim cations in this sample are incorporated into the aluminate structure due to a chemical reaction of the promotor with Al_2O_3. The $E_b(Cs3d_{5/2})$ value of 724.9 eV found for $Ru-Cs^+/Al_2O_3$ also does not contradict to its assignment to caesium aluminate.

The following important conclusion can be derived from the above extensive studies[158–160] of supported ruthenium catalysts of the ammonia synthesis. An analysis of the mechanims of the formation of active sites schematically depicted in Fig. 27 has to take into account the promotor – ruthenium and promotor – support interactions in addition to more common support – ruthenium interactions. Indeed, magnesia, due to its prominent basicity, is expected to be quite inert as regards its reaction with caesium oxides, which are themselves strong bases. This largely facilitates the migration of caesium over the magnesia surface to react with ruthenium particles thus generating active sites for the N_2+H_2 reaction (Fig. 27 *a*). The dissociative adsorption of N_2 should be accelerated on such sites due to a decrease in the electron escape work function.

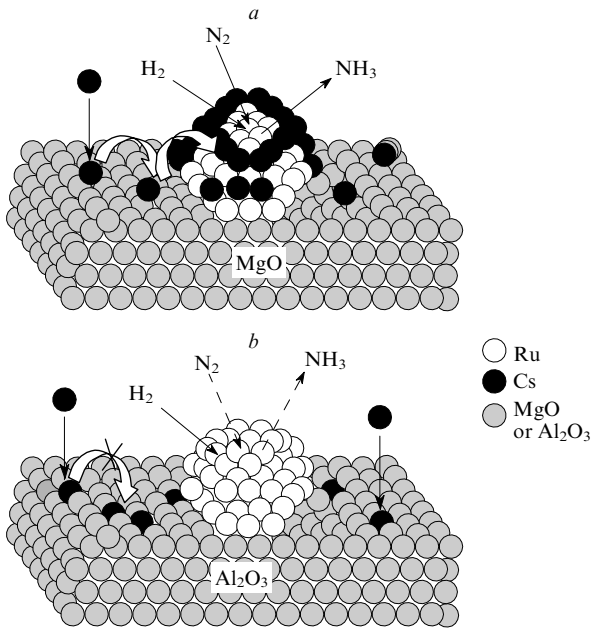


Figure 27. A scheme of interaction of the promotor with the support and active component in the catalysts $Ru-Cs^+/MgO$ and $Ru-Cs^+/Al_2O_3$.

On the contrary, acidic sites present on the alumina surface strongly bind the promotor thus preventing them from the reaction with ruthenium particles (Fig. 27 *b*). Consequently, non-promoted ruthenium particles manifest a lower activity in the dissociative nitrogen adsorption, which determines to the overall low activity of such catalysts in the ammonia synthesis. It is of note that alumina-based catalytic systems can manifest high activity in the ammonia synthesis, but only at high promotor content (promotor : metal $\geqslant$ 3.0).[174] Very likely, at high concentrations, a fraction of the promotor remains unbound to the support and thus capable of ruthenium activation.

Despite the prominent success of the post-reaction analysis of the mechanism of formation of active component in porous catalysts with surface-sensitive techniques, future progress in this field relates to the extensive usage of *in situ* measurements. For instance, the structure of active sites of barium-promoted ruthenium catalysts supported on BN has been determined by *in situ* TEM studies.[176] In the as-prepared catalysts, ruthenium particles were incorporated into boron nitride. TEM micrographs measured under the reaction conditions of the ammonia synthesis reveal restructured catalyst surfaces and support-free ruthenium particles covered with the barium promotor in the form of either amorphous particles or a monolayer coating. It was concluded that barium is an electron promotor for ruthenium.[176]

Additional examples of highly efficient *in situ* XPS investigations into the state of active components in porous catalysts can be found in recent publications by Schlögl *et al.*[177–179]

2. Hydrogen sulfide oxidation of iron-based catalysts

The use of model objects instead of real catalysts for monitoring the formation of active sites becomes inefficient for catalytic reactions involving agressive reaction media. The inadmissibility of agressive gases into UHV chambers due to safety reasons prevents *in situ* measurements thus eliminating one of the most important merits of model experiments, *viz.*, the absence of exposure to air of samples after their activation. This limits the research capabilities to the traditional post-reaction analysis with a necessary comparison of as-prepared, activated and sometimes deactivated catalysts. It is always desirable to avoid exposure to air of the samples upon their transfer from a catalytic reactor to the analytical UHV chamber. This requirement was fullfilled in a study of the formation of active sites of supported iron catalysts for the H_2S oxidation, such as Fe_2O_3/SiO_2 and Fe_2O_3/Al_2O_3.[180, 181]

According to the XPS data, the reaction of the iron-containing catalysts with gas mixtures containing a large fraction of water vapour in addition to hydrogen sulfide and oxygen, gives rise to the sulfidation of surface layers of iron oxide(III) particles.[180, 181] Such a change in the chemical state of the active component was identified by the appearance of a $Fe2p_{3/2}$ component with a binding energy of 708.8 eV, which is typical of FeS_2.[182, 183] At the same time, an intense signal of sulfide ions emerges in the S2p XPS spectra ($E_b \approx 163$ eV). The spectral line attributable to Fe_2O_3 with $E_b(Fe2p_{3/2}) = 711.2$ eV remains dominant in the spectra, which suggests the surface sulfidation of the active component.

A comparison of the XPS results with data on the catalytic activity revealed that oxide forms of the active site catalyse the selective oxidation of H_2S to sulfur, whereas the formation of FeS_2 alters the oxidation pathway. The total oxidation product, SO_2, becomes dominant in this case. It is of note that both the selective and total hydrogen sulfide oxidation are of practical interest, although for different applications. The application of instrumental techniques, such as XPS, to the elucidation of the sulfidation process revealed important details regarding the effects of the support type, precursor

nature, annealing temperature and amount of water on the rate of formation and depth of FeS_2 formation.[180, 181]

V. Development of methods of the purposeful synthesis of highly active catalysts

The purposeful design of catalysts based on the knowledge of the structure of active sites gathered in model studies is an extremely important task, since it allows the easiest verification of the performance of intuitively envisaged active site structures in practice. Indeed, the correctness of the structure–activity relationship adopted in the molecular design enables the development of convenient methods for the synthesis of highly active and selective catalysts with a prolonged service life. Without this knowledge, such methods affording advanced practical catalysts will remain elusive. Instrumental techniques of surface studies within this approach are necessary to control the results of the molecular design aimed at the preparation of active sites with a desirable composition and structure. The productivity of this approach is demonstrated below with some examples.

1. Bimetallic Ni–Au catalyst for the steam reforming of hydrocarbons

The purposeful improvement of Ni catalysts for the steam reforming of hydrocarbons is one of the most striking examples of the efficacy of the fundamental approach to the improvement of the catalyst performance.[184–186] Nickel is widely used as a component of industrial catalysts of the steam reforming of natural gas (primarily, methane). As has been shown, the steam reforming starts with the methane activation on nickel. This is accompanied by the progressive deposition of graphite on the surface of Ni catalyst followed by the growth of filamentous carbon and ultimately by the catalyst deactivation.[187, 188]

The deactivation of Ni catalysts due to the formation of graphite layers on early steps of the catalytic reaction was established unambiguously using TEM. The deactivation of Ni catalysts can be suppressed by introducing minor amounts of hydrogen sulfide into the reaction mixture. Sulfur adsorbed on the Ni particles poisons the catalyst, which, on the one hand, decelerates the overall steam conversion reaction but, on the other hand, inhibits the graphite formation, thus significantly prolonging the service life of the catalyst. Despite some promise of this approach, it has not found wide application since sulfur-contaning compounds poison various catalytical reactions, in particular those combined with the steam reforming into technological scheme, such as ammonia synthesis.

Another possible approach to overcome the problem of the fast deactivation of Ni catalysts in the steam reforming relates to a modification of the active component by, for example, alloying nickel with another metal. The best results are expected for metals forming only surface rather than bulk alloys with nickel. As has been shown by Besenbacher *et al.*[190–192] in an STM study of model objects, nickel indeed forms surface alloys in a series of binary systems, such as nickel–gold. The reason for the formation of this surface alloy is a decrease in the surface tension energy of nickel due to the electron density transfer from the gold atoms to the low-coordinated nickel atoms at the surface. These simple qualitative speculations were supported by quantum chemical calculations at the DFT level, which demonstrated that the bonding of carbon to the nickel atoms having adjacent Au atoms is much weaker than that to Ni atoms in the exclusively nickel environment.

As a result of these model studies,[190–192] the porous Ni–Au catalysts were suggested. They were prepared by depositing 16.5 mass.% of a nickel–gold mixture (0.3% of gold) on the surface of magnesium aluminate.[193] The incorporation of gold atoms in the surface layers of nickel particles yielding a surface alloy was unambiguously confirmed by EXAFS. Further assay of these $Ni(Au)/MgAl_2O_4$ catalysts in the steam reforming of *n*-butane demonstrated a stably high activity of the bimetallic systems in cotrast to the standard nickel catalysts.[193] Butane was used rather than methane due to its easier graphitisation.

Thus, the understanding of the structure–activity relationships indeed enabled the molecular design of advanced nickel-based catalysts for the steam reforming of hydrocarbons characterised by significantly improved stability against deactivation.

2. Nanosized Au/Al_2O_3 catalysts for the low-temperature CO oxidation

The synthesis of Au/Al_2O_3 catalysts for the low-temperature CO oxidation represents yet another example of the purposeful design of an advanced catalyst for specific catalytic processes.[194–196] The molecular design of this system was based on the results of fundamental investigations into the reasons governing the catalytic activity of gold nanoparticles,[120–123] which revealed a pronounced size effect in the activity of Au/TiO_2 catalysts. Taking into account some technological inconvenience of TiO_2 as a support for industrial applications, alumina was chosen as the support material. Therefore, it became necessary to develop efficient methods for the preparation of nanosized gold particles on the surface of alumina particles, including γ- (microspherical particles) and θ-Al_2O_3 (fine powder).[194–196] Three major synthetic procedures were tested: the Deposition-Precipitation (DP), Chemical Liquid-Phase Grafting (CLPG) and Chemical Vapour Deposition (CVD) from volatile gold complexes.

Hexachloroauric acid was selected as a precursor of the active component in the DP synthesis, whereas dimethylgold acetylacetonate was used for CLPG and CVD due to its high volatility, thermal stability [the saturated vapour pressure of $(CH_3)_2Au(acac)$ is 5.5×10^{-4} Torr at 25 °C, while the decomposition point in the solid state is 54 °C] and accessibility.[194]

The mean sizes of gold particles in the catalysts were determined using X-ray diffraction and TEM. X-ray diffraction was also used to control the phase composition of the samples. Since the most intense diffraction peaks of bulk gold (*i.e.*, 111, 200 and 220) overlap with the reflexes of Al_2O_3, the sizes of Au crystallites were determined from the width of the Au(311) peak at $2\theta \approx 78^\circ$ using the Selyakov–Scherrer equation.

Preliminary TEM study of the Au/Al_2O_3 catalysts showed that standard procedures of TEM images measurement appeared unsatisfactory: the Au particles with a diameter smaller than $\leqslant 5$ nm were nearly undistinguishable on the background of the support. Therefore, special techniques of the contrast enhancement were applied. In particular, the use of Fresnel scattering suppression on the Al atoms helped to decrease the brightness of the Al_2O_3 surface background with respect to that Au particles. Furthermore, the TEM micrographs used for the size distribution analysis of the Au particles were obtained in the so-called Z-contrast mode, *i.e.*, at a specific electron collection angle providing that only electrons scattered on the Au atoms contribute to the image. In this mode, the gold particles occur in the micrographs as bright spots on the uniform black background coming from the support and thus the particle size can be determined quite precisely. Typical micrographs of the catalysts prepared by the DP method and annealed at 673 K are shown in Figs. 28 and 29. From a series of TEM micrographs, histograms of the gold particle size distribution were obtained in both cases, which are also shown in Figs 28 and 29.

It is apparent that the Au/θ-Al_2O_3 catalyst (sample *1*, Fig. 28 *a*) mainly contains gold particles with a size of

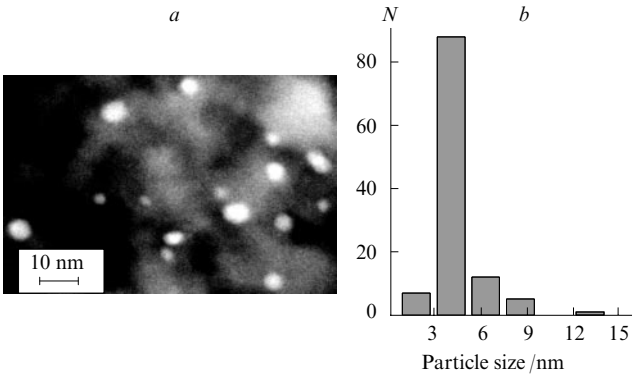


Figure 28. TEM Image of the Au/θ-Al_2O_3 catalyst (sample *1*) (*a*) and the respective Au particle size distribution (*b*) (hereinafter, *N* is the number of particles).
The catalyst was prepared by the deposition precipitation method from Au(III) hydroxo complexes. The image was acquired in the Z-contrast mode. The mean linear diameter of the Au particles is 3.8 nm.

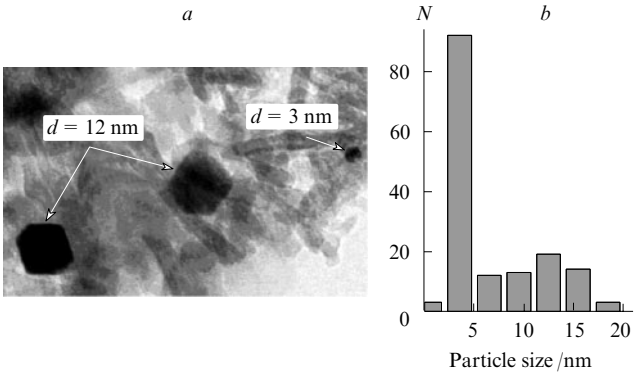


Figure 29. TEM Image of the Au/γ-Al_2O_3 catalyst (sample *2*) (*a*) and the respective Au particle size distribution (*b*).
The catalyst was prepared by the deposition precipitation method from Au(III) hydroxo complexes. The image was acquired in the normal contrast mode. The mean linear diameter of the Au particles is 6.6 nm.

2–4 nm and single particles with a size from 5 nm to 8 nm. The particles are characterised by a nearly spherical shape. The size distribution is relatively narrow and has a Gaussian shape; the mean linear diameter of the Au particles $\langle d_{Au}\rangle$ = 3.8 nm (Fig. 28 *b*). In the case of the Au/γ-Al_2O_3 catalyst (sample *2*, Fig. 29 *a*), the TEM micrographs reveal microaggregates composed of primary globules of the support covered with mainly small gold particles with a size of 2–4 nm. At the same time, larger particles of up to 10–15 nm are also present in the sample. As a result, the size distribution of Au particles in this case is bimodal with two maxima at 4 nm and 12 nm (Fig. 29 *b*).

The mean sizes of Au particles in the Au/Al_2O_3 catalysts determined from TEM and X-ray diffraction data are compared in Table 4. In the case of samples prepared by deposition-precipitation, the mean volume-surface diameter ($\langle d_{vs}\rangle$) of Au particles estimated from TEM was larger than that calculated from the broadening of the Au(311) diffraction line. The maximum discrepancy between the TEM and diffraction estimates is observed for sample *2*. In this case, the contribution of relatively large metal particles into the diffraction broadening is small, although total numbers of small and large particles are comparable according to the TEM estimate.

Table 4. The mean diameters of supported gold particles in the Au/Al_2O_3 catalysts estimated from X-ray diffraction (XRD) and TEM data.

Sample	Preparation method	Support	Au content (mass %)	Mean diameter of Au particles /nm			
				XRD	TEM [a]		
					$\langle d_l\rangle$	$\langle d_s\rangle$	$\langle d_{vs}\rangle$
1	DP	θ-Al_2O_3	1.4	⩽3	3.8 ± 1.3	4.1	4.5
2	DP	γ-Al_2O_3	1.3	6.6	6.6 ± 4.7	8.1	12.5
3	CLPG	γ-Al_2O_3	3.8	12	13.3 ± 2.8	13.6	14.5
4	CVD	γ-Al_2O_3	1.2	>5	20–25		5.6
5	CVD	γ-Al_2O_3	0.7	⩽3	2.9 ± 0.9		3.5

[a] $\langle d_l\rangle = \dfrac{\sum_i f_i d_i}{\sum_i f_i}$, $\langle d_s\rangle = \sqrt{\dfrac{\sum_i f_i d_i^2}{\sum_i f_i}}$ and $\langle d_{vs}\rangle = \dfrac{\sum_i f_i d_i^3}{\sum_i f_i d_i^2}$,
where f_i is the number of particles with a diameter d_i encountered in TEM images.

Sample *3* prepared by the CLPG method from $(CH_3)_2$Au(acac) and annealed at 673 K in air contained predominantly Au particles with a size of 8–18 nm characterised by a normal distribution and single particles with a larger size of ~20 nm (Fig. 30 *b*). This sample was nearly devoid of metal particles with a size ⩽ 5 nm. The mean diameters of Au particles estimated by TEM and X-ray diffraction were nearly identical (see Table 4).

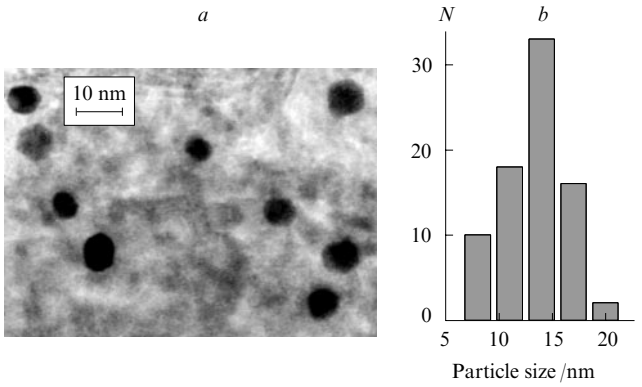


Figure 30. TEM Image of the Au/γ-Al_2O_3 catalyst (sample *3*) (*a*) and the respective Au particle size distribution (*b*).
The catalyst was prepared by the chemical liquid-phase grafting of $(CH_3)_2$Au(acac) on the γ-Al_2O_3 surface. The mean linear diameter of the Au particles is 13 nm.

The chemical vapour deposition was performed according to two procedures. Sample *4* was synthesised by passing $(CH_3)_2$Au(acac) vapour through an immobile layer of γ-Al_2O_3 kept at room temperature. The process was accompanied by a change in the vapour colour indicative of a partial decomposition of the complex by water molecularly adsorbed on the support surface. A chemical analysis of several probes of the sample *4* taken in different places of the reactor showed that the Au concentration progressively decreases along the direction of the gas flow. This gradient indicates that the interaction of $(CH_3)_2$Au(acac) with the surface of γ-Al_2O_3 is too strong. Thus, the CVD procedure was modified in order to prevent the uncontrollable decomposition of the organometallic precursor and provide the uniform distribution of the active component over the support. This modified procedure was

used for the preparation of sample *5*. First, the support was carefully dehydrated by annealing *in vacuo* ($\sim 10^{-7}$ Torr) at 300–350 °C prior to its contact with vapourised $(CH_3)_2Au(acac)$. Second, the deposition was accomplished in a constantly rotating reactor under the quasistationary conditions. The resultant sample was uniformely coloured and the Au concentrations in several probes taken from different places were nearly identical.

According to the TEM studies, sample *4* contained gold particles characterised by a very broad size distribution (from 5 nm to 35 nm), whereas TEM micrographs of sample *5* typically revealed microaggregates of primary γ-Al_2O_3 globules covered with mainly small Au particles of spherical or semispherical shapes with sizes from 2 nm to 4 nm (Fig. 31 *a*), although single larger particles with a diameter 5–10 nm were also present. The size distribution is rather narrow and has a Gaussian shape with a maximum at 2.5–3.0 nm (Fig. 31 *b*).

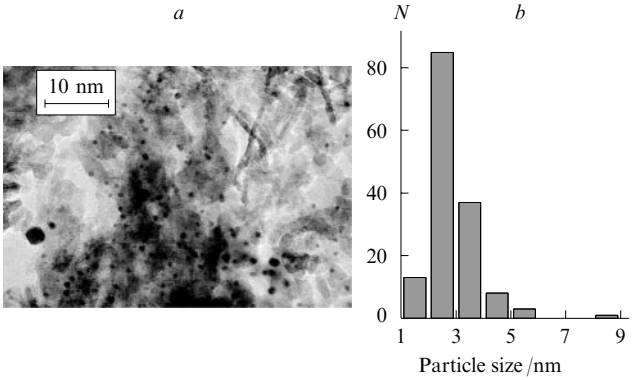


Figure 31. TEM Image of the Au/γ-Al_2O_3 catalyst (sample *5*) (*a*) and the respective Au particle size distribution (*b*).
The catalyst was prepared by the chemical vapour deposition of $(CH_3)_2Au(acac)$ on the γ-Al_2O_3 surface. The mean linear diameter of the Au particles is 3.3 nm.

These Au/Al_2O_3 catalysts prepared by different synthetic routes were assayed in terms of their catalytic activity towards the CO oxidation. The catalytic studies were performed in a plug-flow reactor at 313 K and ambient pressure. The testing conditions were chosen so as to approach the realistic oxidation conditions in a closed room with ordinary humidity and slightly elevated temperature. The composition of the initial reaction medium (IRM) corresponded to air purified from CO. The results obtained are listed in Table 5.

Under the conditions used, samples *1* and *2* demonstrated high catalytic activities in the CO oxidation. The most active Au/θ-Al_2O_3 catalyst (sample *1*) taken in an amount as small as 40–50 mg provided the degree of CO conversion of $\sim$45% at the maximum possible SRM supply rate (400 ml min^{-1}). It was impossible to realise the process for this sample under differential conditions, which resulted in somewhat underestimated reaction rates (see Table 5). The Au/γ-Al_2O_3 catalyst (sample *2*) demonstrated a lower activity probably due to a significantly larger mean size of gold particles in this sample ($\langle d_{vs} \rangle$ = 12.5 nm) as compared to sample *1*.

Sample *3* did not demonstrate any measurable catalytic activity in the CO oxidation over the temperature range of 313–523 K; in the presence of this catalyst, CO_2 lines were detected in the Raman spectra only when temperature was increased to 773 K (the degree of CO conversion was then $\sim$ 2%). Since the mean size of Au particles $\langle d_{vs} \rangle$ in sample *3* is virtually the same as in sample *2* (according to TEM), the observed dramatic difference in the catalytic activity could be attributed to different size distributions of Au particles in these two samples (see Figs 29 *b* and 30 *b*). Sample *2* is characterised by a broad distribution encompassing particles with sizes from 3 nm to 20 nm. Meanwhile, the distribution for sample *3* is much narrower and includes virtually no Au particles smaller than 5 nm. This strongly suggests that in the case of Au/Al_2O_3, the specific catalytic activity exhibits the same size effect as was observed earlier for the Au/TiO_2, Au/Co_3O_4 and Au/Fe_2O_3 systems: the catalytic activity abruptly increases (by several orders of magnitude) with a decrease in the size of Au crystallites down to $d \leqslant 5$ nm.

Table 5. Activities of the Au/Al_2O_3 catalysts prepared by different methods in the CO oxidation measured in a plug-flow reactor at 313 K.

Sample	$\langle d_{vs} \rangle$ [a] /nm	CO conversion level (%) in		Reaction rate [b]
		1 h	7 h	
1	4.5	89	85	47
2	12.5	19	31	7.4
3	12.0 [c]	< 1	< 1	< 0.05
4	5.6	< 1	< 1	< 0.05
5	3.5	24	55	18.7

Notes. The initial reaction mixture compositions: 1 vol.% CO, 2.2 vol.% H_2O, 20 vol.% O_2, the rest is N_2; the volume rate of the initial reaction mixture supply is 100 ml min^{-1}.
[a] Mean volume surface diameter of the Au particles calculated from the TEM data (see Table 4). [b] The unit of measure is mol CO (mol Au)$^{-1}$ s^{-1}. [c] The mean particle diameter calculated from the XRD data.

Studies on the catalytic activity of samples *4* and *5* also demonstrates the size effect. Sample *4* containing only Au particles with a diameter $\geqslant$5 nm demonstrated no measurable activity. In contrast, sample *5* composed of mainly small gold particles of < 5 nm showed a relatively high activity in the CO oxidation. The starting level of CO conversion in the presence of this catalyst at an Au content of 0.7 mass % was 15%. In three hours, the degree of conversion increased to 35% and remained constant at this level until the end of testing. The apparent activation energy (E_a) of the CO oxidation on the catalyst *5* calclulated from the experimental temperature dependence of the reaction rate assuming the Arrhenius-type function is 9.5 kJ mol^{-1}, which is only slightly larger than the respective value of 7 kJ mol^{-1} found by Goodman for model catalysts.[127] (This again proves the close correspondence between model and real catalytic experiments.)

A change in the electronic state of gold atoms during the preparation of the Au/θ-Al_2O_3 catalysts (sample *1*) was studied using Diffuse Reflectance UV-Vis Spectroscopy (DR-UV-Vis).[195] In addition, the plasmon resonance features in the electronic spectra of gold particles with the bulk structure and the electronic spectra of some model Au(III) complexes with the Au–O–Au bonds were simulated theoretically. A colloid suspension of gold containing spherical Au particles with a mean diameter of $\sim$50 nm was used, as the reference sample, which was prepared by heating of an aqueous $HAuCl_4$ solution (0.05 mg Au ml^{-1}) with a 1% solution of sodium citrate. The respective spectra are shown in Fig. 32.[195]

The spectrum of an alkalified $HAuCl_4$ solution (spectrum *1*, Fig. 32) shows an absorption band centred at 48 000 cm^{-1}. Such spectra with one weak ligand–metal charge transfer line in the UV range are characteristic of mononuclear complexes $[AuCl_{4-x}(OH)_x]^-$ with $x = 2$ and 3. According to the literature data, upon treatment of Al_2O_3 with alkalified $HAuCl_4$ solutions, the complexes $[AuCl_2(OH)_2]^-$ and $[AuCl(OH)_3]^-$ react with the surface OH groups of the support resulting in the immobilisation of the Au(III) ions due to the

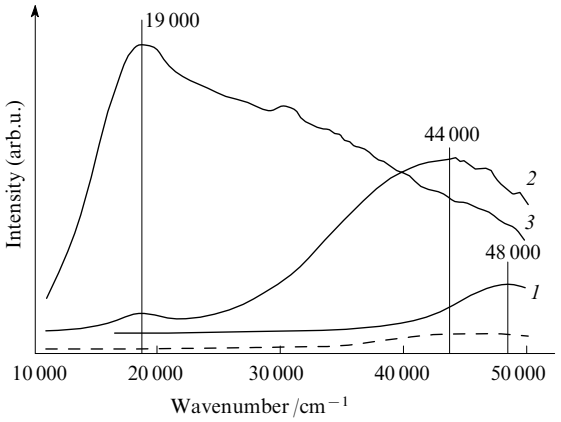


Figure 32. Transmission (*1*) and diffusion reflectance (*2*, *3*) UV-Vis spectra for the Au/θ-Al_2O_3 catalyst and reference samples; (*1*) alkalified aqueous solution of $HAuCl_4$ ([Au] = 0.013 mol litre^{-1}, [OH]/[Au] = 3.8 mol mol^{-1}); (*2*) θ-Al_2O_3 support after treatment with the $HAuCl_4$ solution (conditions *1*) at 70 °C, thorough washing with water and drying; (*3*) sample (*2*) after calcination in air at 400 °C for 4 h (1.5% Au/θ-Al_2O_3 catalyst). The DR-UV-Vis spectrum of the original θ-Al_2O_3 is shown with a dashed line.

formation of the Al—O—Au bonds. A subsequent thorough washing with warm water leads to the removal of the Au(III) ions weakly bound to the support and the hydrolysis of the Au—Cl bonds in the immobilised complexes. The residual Cl content in samples prepared in this way is < 0.01 mass %, according to X-ray fluorescence analysis.[195]

The DR-UV-Vis spectrum of the θ-Al_2O_3 sample treated with an alkalified $HAuCl_4$ solution reveals a new broad absorption band over 35 000 – 50 000 cm^{-1} centred at 44 000 cm^{-1} (spectrum *2*, Fig. 32), which is probably due to chemisorbed Au(III) complexes. The so large width of this band indicates heterogeneous composition of the surface compounds. A shift in the position of the absorption band maximum to lower wavenumber with respect to the spectrum of parent alkalified $HAuCl_4$ solution can be due to exchange interactions between the Au(III) ions immobilised on the Al_2O_3 surface. The exchange interaction implies that the sorbed Au(III) ions are associated, for instance into 'islets' with a high local concentration of grafted complexes with neighbouring metal ions located at a distance of 0.5 – 1 nm from each other.

In addition to the absorption band at 44 000 cm^{-1}, the DR-UV-Vis spectrum of θ-Al_2O_3 treated with an alkalified $HAuCl_4$ solution exhibits an additional weak band at 19 000 cm^{-1} attributed to the plasmon absorption band from gold metal nanoparticles. The appearance of the resonance plasmon line for this sample means that metallic gold is partly formed already upon adsorption or during the washing and/or drying steps. The absorption band at 19 000 cm^{-1} abruptly increases after annealing of the sample in air at 400 °C and a new band at 25 000 – 32 000 cm^{-1} emerges. Since resonance plasmon features cannot be shifted so far to larger wavenumbers, the observation of the band at 25 000 – 32 000 cm^{-1} indicates that the Au/θ-Al_2O_3 sample contains 'ionic' species of gold in addition to metal particles.[195]

The formation of metal oxide clusters and their co-existence with metallic gold was observed earlier in Au/MgO catalysts manifesting high activity in the low-temperature CO oxidation.[197, 198] The application of X-ray absorption techniques EXAFS and XANES to probe the chemical state of gold nanoparticles revealed that both cationic and zero-valence (*i.e.*, metallic) gold co-exist in the functioning catalysts and relative amounts of these two forms depend on the composition of the reaction mixture. Simultaneous measurements of X-ray absorption spectra and the catalytic activity of Au/MgO catalysts in the CO oxidation for reaction media with different reactant ratios made it possible to correlate the reaction rate and relative fractions of the cationic and zero-valence gold. The results of these measurements are shown in Fig. 33. The maximum activity is achieved in the case of Au/MgO catalysts with nearly equal fractions of the ionic and metallic gold.

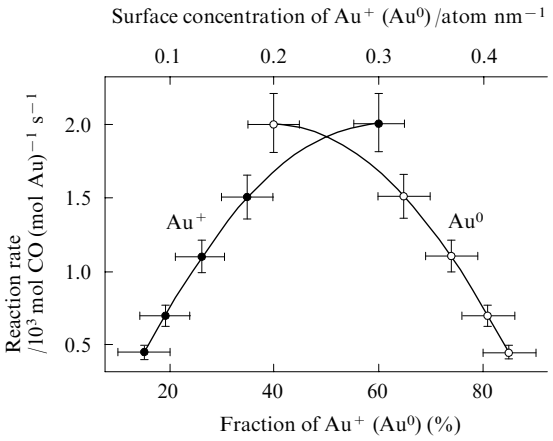


Figure 33. Catalytic activity of the Au/MgO catalyst in the CO oxidation as a function of surface concentrations of cationic and zero-valence gold in the sample.[197]

These results suggest that the activity of the Au/Al_2O_3 catalysts in the low-temperature CO oxidation is due to the associative mechanism of the process similar to that used earlier to rationalise the catalytic action of some metal oxides in this reaction. The associative mechanism of the CO oxidation assumes that a decrease in the apparent activation energy of the catalytic reaction is achieved due to energy-coupled oxidation and reduction of surface oxide metal clusters accompanied by the formation of carbonate structures as key intermediates.

The above data demonstrate a practical potential of the Au/Al_2O_3 catalysts. Indeed, possible areas of application of catalysts providing the low-temperature CO oxidation are extremely broad. These catalysts are of importance for the air purification in closed spaces, solution of the 'cold start' problem in the exhaust gas neutralisation, purification of hydrogen from CO for the use in fuel cells based on proton-conducting membranes, *etc.*

VI. Conclusion

The examples discussed in the present review clearly demonstrate that instrumental techniques for surface studies remain essential for catalytic investigations, since they yield detailed information on the structure of surface sites driving specific catalytic reactions thus helping to establish the structure – activity relationships in heterogeneous catalysts. In parallel, modern trends in surface science require several novel approaches to be included into everyday practice of scientific investigations. In particular, these include:

— *in situ* methods of catalyst characterisation enabling studies exactly under conditions of catalytic reactions (a new term Operando spectroscopy appeared recently to designate this type of experiments);

— techniques for the analysis of nanosized and nanostructured materials (primarily, with a low concentration of an

active component) sensitive to the metal–support interactions (it is the efficient interaction of metal nanoparticles with the support that provides the optimum, from the catalytic perspective size of the active component and its stability against aggregation and deactivation upon sintering);

— methods for the synthesis of nanosized and nanostructured catalysts with a controlled narrow particle size distribution, including both model catalysts on single-crystalline substrates and real catalysts with high specific surface area.

The first approach offers one possible way to address the 'pressure gap' problem, whereas two latter approaches address the 'material gap' problem. The experimental information on the structure of active sites retreived by instrumental methods for surface science will be reliable and relevant to specialists in catalysis for the design of highly active and selective catalysts only provided that both these problems are properly addressed. The costs for the development of so expensive direction as surface science are well warranted by the ultimate practical success in the invention of novel advanced catalysts. Essentially, this concerns research efforts that can result in the establishment of a totally new material and technical basis of chemical and petrochemical industry, where 80% of all processes are nowadays catalytic.

Due to the complexity and expensiveness of the surface science instrumentation, further progress in the field is only possible with a wide cooperation of scientists from diverse disciplines (physicists and chemists, theoreticians and experimentalists, surface scientists and catalysis experts), integration of research capabilities of different centres and laboratories, including international collaborations.

The author is grateful to the personnel of the Surface Science Laboratory at the G K Boreskov Institute of Catalysis, Siberian Branch of the Russian Academy of Sciences V V Kaichev, A V Kalinkin, R I Kvon, Yu V Larichev, B L Moroz, A V Pashis, I P Prosvirin, P A Pyryaev, A M Sorokin and M Yu Smirnov as well as to colleagues from other laboratories and foreign colleagues (see references) for the help in the discussion and implementation of experiments bridging surface science and catalysis. The author also thanks the Russian Foundation for Basic Reseach for the long-term financial support of the work (Project Nos 96-03-33 891, 01-03-32 853, 03-03-89 012-NWO, 06-03-33 020 and 07-03-00 931).

References

1. *Surf. Sci.* **299**/**300** 837 (1994)
2. T Engel, G Ertl *Adv. Catal.* **28** 1 (1979)
3. M W Roberts, C S McKee *Chemistry of the Metal–Gas Interface* (Oxford: Clarendon Press, 1978)
4. G A Somorjai *Surface Chemistry and Catalysis* (New York: Wiley, 1994)
5. A Böttcher, H Niehus, S Schwegmann, H Over, G Ertl *J. Phys. Chem. B* **101** 11185 (1997)
6. H Over, Y D Kim, A P Seitsonen, S Wendt, E Lundgren, M Schmid, P Varga, A Morgante, G Ertl *Science* **287** 1474 (2000)
7. H Over, A P Seitsonen, E Lundgren, M Wiklund, J N Andersen *Chem. Phys. Lett.* **342** 467 (2001)
8. C T Campbell, M T Paffett *Surf. Sci.* **139** 396 (1984)
9. C T Campbell, M T Paffett *Surf. Sci.* **143** 517 (1984)
10. C T Campbell *Surf. Sci.* **157** 43 (1985)
11. R W Joyner, M W Roberts, K Yates *Surf. Sci.* **87** 501 (1979)
12. R W Joyner, M W Roberts *Chem. Phys. Lett.* **60** 459 (1979)
13. A I Boronin, V I Bukhtiyarov, A L Vishnevskii, G K Boreskov, V I Savchenko *Surf. Sci.* **201** 195 (1988)
14. M Boudart *Adv. Catal.* **20** 153 (1969)
15. M Che, C O Bennett *Adv. Catal.* **36** 55 (1989)
16. H Poppa *Catal. Rev. Sci. Eng.* **35** 359 (1993)
17. M Bäumer, H-J Freund *Prog. Surf. Sci.* **61** 127 (1999)
18. C R Henry *Surf. Sci. Rep.* **31** 231 (1998)
19. A A Kolmakov, D W Goodman, in *Chapter in Quantum Phenomena in Clusters and Nanostructures* (Eds S V Khann, A W Castleman) (Berlin: Springer-Verlag Physics Series in Cluster Physics, 2003) p. 159
20. V I Bukhtiyarov, M G Slin'ko *Usp. Khim.* **70** 167 (2001) [*Russ. Chem. Rev.* **70** 147 (2001)]
21. V I Bukhtiyarov, in *Interfacial Science 'Chemistry for the 21st Century Monograph'* (Ed. M W Roberts) (Oxford: Blackwell, 1997) p. 109
22. J Szanyi, W K Kuhn, D W Goodman *J. Vac. Sci. Technol., A* **11** 1969 (1993)
23. E Ozensoy, D C Meier, D W Goodman *J. Phys. Chem. B* **106** 9367 (2002)
24. O Rodrígues de la Fuente, M Borasio, P Galletto, G Rupprechter, H-J Freund *Surf. Sci.* **566–568** 740 (2004)
25. P S Cremer, B J McIntyre, M Salmeron, Y-R Shen, G A Somorjai *Catal. Lett.* **34** 11 (1995)
26. G A Somorjai, G Rupprechter *J. Phys. Chem. B* **103** 1623 (1999)
27. G Rupprechter, T Dellwig, H Unterhalt, H-J Freund *J. Phys. Chem. B* **105** 3797 (2001)
28. G Rupprechter *Phys. Chem. Chem. Phys.* **3** 4621 (2001)
29. A Knop-Gericke, M Hävecker, Th Shedel-Niedrig, R Schlögl *Top. Catal.* **15** 27 (2001)
30. V I Bukhtiyarov, M Hävecker, V V Kaichev, A Knop-Gericke, R W Mayer, R Schlögl *Catal. Lett.* **74** 121 (2001)
31. H Bluhm, M Hävecker, E Kleimenov, A Knop-Gericke, A Liskowski, R Schlögl, D S Su *Top. Catal.* **23** 99 (2003)
32. H J Ruppender, M Grunze, C W Kong, M Wilmers *Surf. Interface Anal.* **15** 245 (1990)
33. D F Ogletree, H Bluhm, G Lebedev, C S Fadley, Z Hussain, M Salmeron *Rev. Sci. Instrum.* **73** 3872 (2002)
34. I P Prosvirin, E P Tikhomirov, A M Sorokin, V V Kaichev, V I Bukhtiyarov *Kinet. Katal.* **44** 724 (2003) [a]
35. H Bluhm, M Hävecker, A Knop-Gericke, E Kleimenov, R Schlögl, D Teschner, V I Bukhtiyarov, D F Ogletree, M Salmeron *J. Phys. Chem. B* **108** 14340 (2004)
36. V I Bukhtiyarov, V V Kaichev, I P Prosvirin *Top. Catal.* **32** 3 (2005)
37. B J McIntyre, M Salmeron, G A Somorjai *Science* **265** 1415 (1994)
38. B L M Hendriksen, J W M Frenken *Phys. Rev. Lett.* **89** 46101 (2002)
39. M A Vannice *J. Catal.* **37** 449 (1975)
40. P Biloen, W M H Sachtler *Adv. Catal.* **30** 165 (1981)
41. A T Bell *Catal. Rev. Sci. Eng.* **23** 203 (1981)
42. G Henrici-Olive, S Olive *The Chemistry of the Catalysed Hydrogenation of Carbon Monoxide* (Berlin: Springer, 1984)
43. R B Anderson *The Fischer–Tropsch Synthesis* (London: Academic Press, 1984)
44. E V Slivinskii, Yu P Voitsekhovskii *Usp. Khim.* **58** 94 (1989) [*Russ. Chem. Rev.* **58** 57 (1989)]
45. S Surnev, M Sock, M G Ramsey, F P Netzer, M Wiklund, M Borg, J N Anderson *Surf. Sci.* **470** 171 (2000)
46. V V Kaichev, I P Prosvirin, V I Bukhtiyarov, H Unterhalt, G Rupprechter, H-J Freund *J. Phys. Chem. B* **107** 3522 (2003)
47. D L Doering, H Poppa, J T Dickinson *J. Catal.* **73** 104 (1982)
48. V Matolín, E Gillet *Surf. Sci.* **238** 75 (1990)
49. I Stará, V Matolín *Surf. Sci.* **313** 99 (1994)
50. H Dropsch, M Baerns *Appl. Catal., A* **158** 163 (1997)
51. K Christmann, J E Demuth *J. Chem. Phys.* **76** 6308 (1982)
52. J L Davis, M A Barteau *Surf. Sci.* **235** 235 (1990)
53. F Solymosi, A Berkó, Z Tóth *Surf. Sci.* **285** 197 (1993)
54. J-J Chen, Z-C Jaing, Y Zhou, B R Chakraborty, N Winograd *Surf. Sci.* **328** 248 (1995)
55. M Rebholz, V Matolin, R Prins, N Kruse *Surf. Sci.* **251** 1117 (1991)
56. N M Rodriguez, P E Anderson, A Wootsch, U Wild, R Schlögl, Z Paal *J. Catal.* **197** 365 (2001)
57. M Barber, J A Connor, M F Guest, M B Hall, I H Hillier, W N E Meredith *Faraday Discuss. Chem. Soc.* **54** 219 (1972)
58. H Lüth, G W Rubloff, W D Grobmann *Surf. Sci.* **63** 325 (1977)

59. J L Davis, M A Barteau *Surf. Sci.* **187** 387 (1987)
60. N Kruse, M Rebholz, V Matolin, G K Chuah, J H Block *Surf. Sci.* **238** L457 (1990)
61. M Rebholz, N Kruse *J. Chem. Phys.* **95** 7745 (1991)
62. A K Bhattacharya, M A Chesters, M E Pemble, N Sheppard *Surf. Sci.* **206** L845 (1988)
63. R J Levis, J Zhicheng, N Winograd *J. Am. Chem. Soc.* **111** 4605 (1989)
64. X Guo, L Hanley, J T Yates Jr *J. Am. Chem. Soc.* **111** 3155 (1989)
65. C J Zhang, P Hu *J. Chem. Phys.* **115** 7182 (2001)
66. S Schauermann, J Hoffmann, V Johánek, J Hartmann, J Libuda, H-J Freund *Angew. Chem., Int. Ed.* **41** 2532 (2002)
67. M Morkel, V V Kaichev, G Rupprechter, H-J Freund, I P Prosvirin, V I Bukhtiyarov *J. Phys. Chem. B* **108** 12955 (2004)
68. V V Kaichev, V I Bukhtiyarov, G Ruprekhter, H-J Freund *Kinet. Katal.* **46** 288 (2005) [a]
69. J Szanyi, W K Kuhn, D W Goodman *J. Phys. Chem.* **98** 2978 (1994)
70. J A Gates, L L Kesmodel *J. Catal.* **83** 437 (1983)
71. S K Desai, M Neurock, K Kourtakis *J. Phys. Chem. B* **106** 2559 (2002)
72. R D Ramsier, K-W Lee, J T Yates Jr *Surf. Sci.* **322** 243 (1995)
73. P Schilbe, D Farías, K H Rieder *Chem. Phys. Lett.* **281** 366 (1997)
74. G Rupprechter, V V Kaichev, H Unterhalt, M Morkel, V I Bukhtiyarov *Appl. Surf. Sci.* **235** 26 (2004)
75. V V Kaichev, V I Bukhtiyarov, M Hävecker, A Knop-Gerike, R W Mayer, R Schlögl *Kinet. Katal.* **44** 471 (2003)
76. V I Bukhtiyarov, M Hävecker, V V Kaichev, A Knop-Gericke, R W Mayer, R Schlögl *Phys. Rev. B* **67** 235422 (2003)
77. V I Bukhtiyarov, A I Nizovskii, H Bluhm, M Hävecker, E Kleimenov, A Knop-Gericke, R Schlögl *J. Catal.* **238** 260 (2006)
78. R A van Santen, H P C E Kuipers *Adv. Catal.* **35** 265 (1987)
79. V I Bukhtiyarov, A I Boronin, I P Prosvirin, V I Savchenko *J. Catal.* **150** 262 (1994)
80. F J Williams, D P C Bird, A Palermo, A K Santra, R M Lambert *J. Am. Chem. Soc.* **126** 8509 (2004)
81. S Linic, M A Barteau *J. Am. Chem. Soc.* **124** 310 (2003)
82. C Stegelmann, N C Schiødt, C T Campbell, P Stoltze *J. Catal.* **221** 630 (2004)
83. W Lindinger, A Hansel, A Jordan *Chem. Soc. Rev.* **27** 347 (1998)
84. M A Barteau, R J Madix *The Chemical Physics of Solid Surfaces and Heterogeneous Catalysis* Vol. 4. (Eds D A King, D P Woodruff) (Amsterdam: Elsevier, 1982) Ch. 4
85. K Siegbahn, C Nordling, G Johansson, J Hedman, P F Hedén, K Hamrin, U Gelius, T Bergmark, L O Werme, R Manne, Y Baer *ESCA Applied to Free Molecules* (Amsterdam: North-Holland, 1969)
86. X Bao, M Muhler, Th Schedel-Niedrig, R Schlögl *Phys. Rev. B* **54** 2249 (1996)
87. Th Schedel-Niedrig, X Bao, M Muhler, R Schlögl *Ber. Bunsen-Ges. Phys. Chem. Chem. Phys.* **101** 994 (1997)
88. C T Campbell *J. Catal.* **94** 436 (1985)
89. V I Bukhtiyarov, I P Prosvirin, R I Kvon *Surf. Sci.* **320** L47 (1994)
90. W M H Sachtler, C Backx, R A van Santen *Catal. Rev. Sci. Eng.* **23** 127 (1981)
91. E A Carter, W A Goddard III *J. Catal.* **112** 80 (1988)
92. E A Carter, W A Goddard III *Surf. Sci.* **209** 243 (1989)
93. J Stöhr *Springer Series in Surface Sciences* Vol. 25 (Berlin, Heidelberg, New York: Springer, 1992)
94. F M F de Groot, M Grioni, J C Fuggle, J Ghijsen, G A Sawatzky, H Petersen *Phys. Rev. B* **40** 5715 (1989)
95. J Purans, A Kuzmin, Ph Parent, C Laffon *Physica B* **259 – 261** 1157 (1999)
96. P Behrens *Solid State Commun.* **81** 235 (1992)
97. P Behrens, S Aβmann, U Bilow, C Linke, M Jansen *Z. Anorg. Allg. Chem.* **625** 111 (1999)
98. A Deb, A K Chatterijee *J. Phys.: Condens. Matter* **10** 11719 (1998)
99. A Knop-Gericke, M Hävecker, Th Shedel-Niedrig, R Schlögl *Top. Catal.* **10** 187 (2000)
100. G Rovida, F Pratesi *Surf. Sci.* **52** 542 (1975)
101. H A Engelhadt, D Menzel *Surf. Sci.* **57** 591 (1976)
102. M Pascal, C L A Lamont, P Baumgärtel, R Terborg, J T Hoeft, O Schaff, M Polcik, A M Bradshaw, R L Toomes, D P Woodruff *Surf. Sci.* **464** 83 (2000)
103. V I Bukhtiyarov, V V Kaichev, I P Prosvirin *J. Chem. Phys.* **111** 2169 (1999)
104. C I Carlisle, T Fujimoto, W S Sim, D A King *Surf. Sci.* **470** 15 (2000)
105. I L Zilberberg, M A Milov, G M Zhidomirov *Zh. Strukt. Khim.* **40** 422 (1999) [b]
106. M A Milov, I L Zilberberg, S Ph Ruzankin, G M Zhidomirov *J. Mol. Catal. A: Chem.* **158** 309 (2000)
107. A Knop-Gericke, F M F de Groot, J A van Bookhoven, T Ressler *In Situ Spectroscopy of Catalysis* (Ed. B M Weckhuysen) (New York: American Sci. Publ., 2006) Ch. 8
108. P L Hansen, S Helveg, A K Datye *Adv. Catal.* **50** 77 (2006)
109. J V Lauritsen, F Besenbacher *Adv. Catal.* **50** 97 (2006)
110. C Lamberti, E Groppo, G Spoto, S Bordiga, A Zecchina *Adv. Catal.* **51** 1 (2007)
111. G Rupprechter *Adv. Catal.* **51** 133 (2007)
112. F Rumpf, H Poppa, M Boudart *Langmuir* **4** 722 (1988)
113. T Engel, G Ertl *J. Chem. Phys.* **69** 1267 (1978)
114. E I Altman, R J Gorte *Surf. Sci.* **195** 392 (1988)
115. M Herskowitz, R Holliday, M B Cutlip, C N Kenney *J. Catal.* **74** 408 (1982)
116. E I Altman, R J Gorte *Surf. Sci.* **172** 71 (1986)
117. S H Oh, C C Eickel *J. Catal.* **128** 526 (1991)
118. M Haruta *Catal. Today* **36** 153 (1997)
119. G C Bond, D T Thomson *Catal. Rev. Sci. Eng.* **41** 319 (1999)
120. M Haruta, S Tsubota, T Kobayashi, H Kageyama, M J Genet, B Delmon *J. Catal.* **144** 175 (1993)
121. G R Bamwenda, S Tsubota, T Nakamura, M Haruta *Catal. Lett.* **44** 83 (1997)
122. M Valden, X Lai, D W Goodman *Science* **281** 1647 (1998)
123. M Valden, S Pak, X Lai, D W Goodman *Catal. Lett.* **56** 7 (1998)
124. C Xu, X Lai, G W Zajac, D W Goodman *Phys. Rev. B* **56** 13464 (1997)
125. D C Meier, V Bukhtiyarov, D W Goodman *J. Phys. Chem. B* **107** 12668 (2003)
126. D C Meier, D W Goodman *J. Am. Chem. Soc.* **126** 1892 (2004)
127. M S Chen, D W Goodman *Catal. Today* **111** 22 (2006)
128. F Cosandey, T E Madey *Surf. Rev. Lett.* **8** 73 (2001)
129. C T Campbell, S C Parker, D E Starr *Science* **298** 811 (2002)
130. H Hovel, B Grimm, M Bodecker, K Fieger, B Reihl *Surf. Sci.* **463** L603 (2000)
131. N Nilius, M Kulawik, H P Rust, H J Freund *Surf. Sci.* **572** 347 (2004)
132. A V Kalinkin, A V Pashis, V I Bukhtiyarov *React. Kinet. Catal. Lett.* **77** 255 (2002)
133. A V Kalinkin, A V Pashis, V I Bukhtiyarov *React. Kinet. Catal. Lett.* **78** 107 (2003)
134. A V Kalinkin, A V Pashis, V I Bukhtiyarov *React. Kinet. Catal. Lett.* **78** 121 (2003)
135. A V Kalinkin, A V Pashis, V I Bukhtiyarov *Kinet. Katal.* **48** 314 (2007) [a]
136. V I Bukhtiyarov, I P Prosvirin, R I Kvon, S N Goncharova, B S Bal'zhinimaev *J. Chem. Soc., Faraday Trans.* 2323 (1997)
137. V I Bukhtiyarov, V V Kaichev *J. Mol. Catal. A: Chem.* **158** 167 (2000)
138. V I Bukhtiyarov *Kinet. Katal.* **44** 457 (2003) [a]
139. M Yu Smirnov, A V Kalinkin, A V Pashis, A M Sorokin, A S Noskov, V I Bukhtiyarov, K S Kharas, M A Rodkin *Kinet. Katal.* **44** 629 (2003) [a]
140. M Yu Smirnov, A V Kalinkin, A V Pashis, A M Sorokin, A S Noskov, K C Kharas, V I Bukhtiyarov *J. Phys. Chem. B* **109** 11712 (2005)
141. S H Oh, J E Carpenter *J. Catal.* **98** 178 (1986)
142. Y Cai, H G Stenger, C E Lyman *J. Catal.* **161** 123 (1996)
143. J Siera, F Rutten, B E Nieuwenhuys *Catal. Today* **10** 353 (1991)

144. F C M van Delft, J Siera, B E Nieuwenhuys *Surf. Sci.* **208** 365 (1989)
145. S B Schwartz, L D Schmidt, G B Fisher *J. Phys. Chem.* **90** 6194 (1986)
146. V I Bukhtiyarov, A F Carley, L A Dollard, M W Roberts *Surf. Sci.* **381** L605 (1997)
147. V I Bukhtiyarov, V V Kaichev, E A Podgornov, I P Prosvirin *Catal. Lett.* **57** 233 (1999)
148. R A van Santen, C P M de Groot *J. Catal.* **98** 530 (1986)
149. A V Khasin *Kinet. Katal.* **34** 42 (1993) [a]
150. R B Grant, R M Lambert *J. Catal.* **92** 364 (1985)
151. D J Sajkowski, M Boudart *Catal. Rev. Sci. Eng.* **29** 325 (1987)
152. S N Goncharova, E A Paukshtis, B S Balzhnimaev *Appl. Catal., A* **126** 67 (1995)
153. D A Bulushev, E A Paukshtis, Yu N Nogin, B S Balzhinimaev *Appl. Catal., A* **123** 301 (1995)
154. B S Balzhinimaev, V I Zaikovskii, L G Pinaeva, A V Romanenko, G V Ivanov *Kinet. Katal.* **39** 775 (1998) [a]
155. H Dietrich, P Geng, K Jakobi, G Ertl *J. Chem. Phys.* **104** 375 (1996)
156. K Jakobi, H Dietrich, G Ertl *Appl. Surf. Sci.* **121** 558 (1997)
157. K Jakobi *Phys. Status Solidi A* **177** 37 (2000)
158. Yu V Larichev, B L Moroz, I P Prosvirin, V A Likholobov, V I Bukhtiyarov *Chem. Sust. Develop.* **11** 155 (2003)
159. Yu V Larichev, I P Prosvirin, D A Shlyapin, N B Shitova, P G Tsyrul'nikov, V I Bukhtiyarov *Kinet. Katal.* **46** 635 (2005) [a]
160. Yu V Larichev, B L Moroz, E M Moroz, V I Zaikovskii, S M Yunusov, E S Kalyuzhnaya, V B Shur, V I Bukhtiyarov *Kinet. Katal.* **46** 940 (2005) [a]
161. P Moggi, G Predieri, A Maione *Catal. Lett.* **79** 7 (2002)
162. F Rosowski, A Hornung, O Hinrichsen, D Herein, M Muhler, G Ertl *Appl. Catal., A* **151** 443 (1997)
163. K Aika, K Shimazaki, Y Hattori, A Ohya, S Ohshima, K Shirota, A Ozaki *J. Catal.* **92** 305 (1985)
164. T Hikita, K-i Aika, T Onishi *Catal. Lett.* **4** 157 (1990)
165. M G Cattania, F Parmigiani, V Ragani *Surf. Sci.* **211 – 212** 1097 (1989)
166. C D Wagner, in *Practical Surface Analysis* Vol. 1 (Eds D Briggs, M P Seach) (New York: Wiley, 1990) p. 602
167. T L Barr *Crit. Rev. Anal. Chem.* **22** 229 (1991)
168. V I Bukhtiyarov, I P Prosvirin, R I Kvon *J. Electron. Spectrosc. Relat. Phenom.* **77** 7 (1996)
169. C C Hwang, K S An, R J Park, J S Kim, J B Lee, C Y Park, S B Lee, A Kimura, A Kakizaki *J. Electron. Spectrosc. Relat. Phenom.* **88** 733 (1998)
170. G Ebbinghaus, A Simon *Chem. Phys.* **43** 117 (1997)
171. S J Yang, C W Bates *Appl. Phys. Lett.* **36** 675 (1980)
172. J Hrbek, Y W Yang, J A Rodriguez *Surf. Sci.* **296** 164 (1993)
173. E A Podgornov, I P Prosvirin, V I Bukhtiyarov *J. Mol. Catal. A: Chem.* **158** 337 (2000)
174. P Moggi, G Albanesi, G Predieri, G Spoto *Appl. Catal., A* **123** 145 (1995)
175. C J H Jacobsen, S Dahl, P L Hansen, E Törnqvist, L Jensen, H Topsøe, D V Prip, P B Møenhaug, I Chorkendorf *J. Mol. Catal. A: Chem.* **163** 19 (2000)
176. T W Hansen, J B Wagner, P L Hansen, S Dahl, H Topsøe, C J H Jacobsen *Science* **294** 1508 (2001)
177. D Teschner, A Pestryakov, E Kleimenov, M Hävecker, H Bluhm, H Sauer, A Knop-Gericke, R Schlögl *J. Catal.* **230** 186 (2005)
178. E Kleimenov, H Bluhm, M Hävecker, A Knop-Gericke, A Pestryakov, D Teschner, J A Lopez-Sanchez, J K Bartley, G J Hutchings, R Schlögl *Surf. Sci.* **575** 181 (2005)
179. O Pozdnyakova, D Teschner, A Wootsch, J Krohnert, B Steinhauer, H Sauer, L Toth, F C Jentoft, A Knop-Gericke, Z Paal, R Schlögl *J. Catal.* **237** 1 (2006)
180. G A Bukhtiyarova, N S Sakaeva, V A Varnek, E B Burgina, L M Plyasova, V I Bukhtiyarov, V V Kaichev, B P Zolotovskii *Khim. Interes. Ustoich. Razvitiya* **7** 359 (1999) [c]
181. G A Bukhtiyarova, V I Bukhtiyarov, N S Sakaeva, V V Kaichev, B P Zolotovskii *J. Mol. Catal. A: Chem.* **158** 251 (2000)
182. P C J Graat, M A J Somers *Appl. Surf. Sci.* **100 – 101** 36 (1996)
183. M Descostes, F Mercier, N Thoromat, C Beaucaire, M Gautier-Soyer *Appl. Surf. Sci.* **165** 288 (2000)
184. J R Rostrup-Nielsen, J Sehested, J K Nørskov *Adv. Catal.* **47** 65 (2002)
185. J R Rostrup-Nielsen, in *Catalysis: Science and Technology* Vol. 5 (Eds J R Anderson, M Boudart) (Berlin: Springer, 1984) p. 1
186. J R Rostrup-Nielsen, T Rostrup-Nielsen *CATTECH* **6** 150 (2002)
187. S Helveg, C López-Cartes, J Sehested, P L Hansen, B S Clausen, J R Rostrup-Nielsen, F Abild-Pedersen, J K Nørskov *Nature (London)* **427** 426 (2004)
188. H S Bengaard, J K Nørskov, J Sehested, B S Clausen, L P Nielsen, A M Molenbroek, J R Rostrup-Nielsen *J. Catal.* **209** 365 (2002)
189. J R Rostrup-Nielsen *J. Catal.* **85** 31 (1984)
190. L P Nielsen, F Besenbacher, I Stensgaard, E Lægsgaard, C Engdahl, P Stoltze, K W Jacobsen, J K Nørskov *Phys. Rev. Lett.* **71** 754 (1993)
191. F Besenbacher, L P Nielsen, P T Sprunger *Chemical Physics of Solid Surfaces and Heterogeneous Catalysis* (Amsterdam: Elsevier, 1997) Ch. 10
192. F Besenbacher, I Chorkendorff, B S Clausen, B Hammer, A M Molenbroek, J K Nørskov, I Stensgaard *Science* **279** 1913 (1998)
193. J V Lauritsen, R T Vang, F Besenbacher *Catal. Today* **111** 34 (2006)
194. P P Semyannikov, B L Moroz, S V Trubin, G I Zharkova, P A Pyryaev, M Yu Smirnov, V I Bukhtiyarov *Zh. Strukt. Khim.* **47** 473 (2006) [b]
195. V F Anufrienko, B L Moroz, T V Larina, S F Ruzankin, V I Bukhtiyarov, V N Parmon *Dokl. Akad. Nauk* **413** 493 (2007) [d]
196. S B Erenburg, B L Moroz, N V Bausk, V I Bukhtiyarov, S Nikitenko *Nucl. Instrum. Methods Phys. Res., Sect. A* **575** 105 (2007)
197. J Guzman, B C Gates *J. Am. Chem. Soc.* **126** 2672 (2004)
198. J Guzman, B C Gates *J. Phys. Chem. B* **106** 7659 (2002)

[a] — *Kinet. Catal. (Engl. Transl.)*
[b] — *J. Struct. Chem. (Engl. Transl.)*
[c] — *Chem. Sust. Develop. (Engl. Transl.)*
[d] — *Dokl. Chem. (Engl. Transl.)*